

Extratropical Atmosphere-Ocean Variability in CCSM3

Michael Alexander¹, Jeffrey Yin², Grant Branstator², Antonietta Capotondi¹, Christophe Cassou³,
Richard Cullather⁴, Young-oh Kwon², Joel Norris⁵, James Scott¹, Ilana Wainer⁶

1 NOAA-CIRES Climate Diagnostics Center, Boulder, Colorado

2 National Center for Atmospheric Research, Boulder, Colorado

3 CERFACS-SUC, Climate Modelling and Global Change Team, Toulouse, France

4 Lamont-Doherty Earth Observatory, Columbia University, Palisades, NY

5 Scripps Institution of Oceanography, La Jolla, CA

6 Department of Physical Oceanography, University of São Paulo, São Paulo, Brazil

For JCLIM CCSM Special Issue

Submitted January 2005

Corresponding Author:

Michael Alexander

NOAA/CIRES, Climate Diagnostics Center

Mail code: R/CDC1

325 Broadway

Boulder, CO 80305

Michael.Alexander@noaa.gov

Abstract

Extratropical atmosphere-ocean variability over the Northern Hemisphere of the Community Climate System Model version 3 (CCSM3) is examined and compared to observations. Results are presented for an extended control integration with horizontal resolution of T85 (1.4°) for the atmosphere and land and $\sim 1^\circ$ for the ocean and sea-ice.

The mean storm track, the leading modes of storm track variability and the relationship of the latter to tropical and midlatitude sea surface temperature (SST) anomalies are fairly well simulated in CCSM3. The positive correlations between extratropical SST and low-cloud anomalies in summer are reproduced by the model, but there are clear biases in the relationship between clouds and the near surface meridional wind. The model accurately represents the circulation anomalies associated with the jet stream waveguide, the Pacific North American (PNA) pattern, and fluctuations associated with the Aleutian low, including how the latter two features are influenced by El Niño/Southern Oscillation (ENSO). CCSM3 has a reasonable depiction of the Pacific Decadal Oscillation (PDO), but it is not strongly connected to tropical Pacific SSTs as found in nature. There are biases in the position of the North Atlantic Oscillation (NAO) and other Atlantic regimes, as the mean Icelandic low in CCSM3 is stronger and displaced southeastward relative to observations.

Extratropical ocean processes in CCSM3 clearly influence climate variability. As in observations, the model includes the “reemergence mechanism” where seasonal variability in mixed layer depth (MLD) allows SST anomalies to recur in consecutive winters without persisting through the intervening summer. Remote wind stress curl anomalies drive thermocline variability in the Kuroshio-Oyashio Extension region which influences SST, sur-

face heat flux anomalies and the local wind field. The interior ocean pathways connecting the subtropics to the equator in both the Pacific and Atlantic are less pronounced than in nature or in ocean-only simulations forced by observed atmospheric conditions, and water originating in the North Atlantic does not appear to reach the equator via either western boundary or interior pathways in CCSM3.

1. Introduction

Extratropical atmosphere-ocean processes exhibit variability on a broad range of time scales, e.g. the intensity and path of storms change daily while ocean currents can fluctuate over decades or more. These processes vary with the seasons, influence large-scale patterns of climate variability and are linked to each other in complex ways. Many features of the extratropical atmosphere and ocean system are influenced by local air-sea interaction and remote teleconnections through their imprint on sea surface temperature (SST). The ability of climate models to simulate important aspects of the extratropical climate system, including storm tracks, clouds, large-scale atmospheric circulation anomalies and upper ocean mixing and circulation, is critical to our ability to understand and predict climate variability and change. There are several benefits to using coupled general circulation models (GCMs) to explore climate variability, including the archival of complete and dynamically consistent fields, many of which are difficult to measure in nature, and the ability to perform long simulations to isolate climate signals from noise. Here we explore atmospheric and oceanic processes and their influence on Northern Hemisphere variability on synoptic to decadal time scales in the Community Climate System Model version 3 (CCSM3).

Chang et al. (2002) noted the fundamental role of storm tracks in the climate system; they generate much of the day to day weather variability in midlatitudes and are closely linked to the planetary-scale flow. Changes in the position and strength of the storm tracks can force the ocean via changes in the surface heat fluxes, which can exceed 1000 Wm^{-2} in the vicinity of intense extratropical cyclones (Neiman and Shapiro 1993) and may respond

to the ocean via the influence of the SST gradient on the low-level atmospheric baroclinicity (Nakamura et al. 1997).

While storm tracks are substantially weaker in summer than in winter, atmospheric fluctuations can still have a substantial impact on SSTs, as the surface solar and latent heat flux anomalies are large and the ocean mixed layer is shallow. Weare (1994) and Norris and Leovy (1994) noted that total and low-level cloud anomalies are negatively correlated with SST anomalies, which implies a positive feedback: increased cloud cover favors cooler SST by reducing surface insolation, while cooler SST favors more stratiform cloud cover by promoting a shallow and moist atmospheric boundary layer (Norris et al. 1998; Frankignoul and Kestenare 2002; Park et al. 2004). The negative correlations are especially pronounced between 25°N-40°N, where the mean meridional gradients in SST and cloud amount are strong.

During both summer and winter atmospheric teleconnections from remote locations can influence extratropical atmosphere-ocean variability. Principal among these is the “atmospheric bridge”, where SST anomalies in the tropical Pacific associated with El Niño/Southern Oscillation (ENSO) influence the North Pacific and other ocean basins via changes in the atmospheric circulation (e.g. Alexander et al. 2002 and the references therein; Alexander et al. 2004; Deser et al. 2005). There are also midlatitude sources of variability. Large-scale patterns of atmospheric variability, such as the North Atlantic Oscillation (NAO), which derive most of their energy from internal atmospheric processes, can drive changes in the underlying ocean via surface heat and momentum fluxes (Cayan 1992; Iwasaka and Wallace 1995). Another candidate for a midlatitude influence on the extratropical oceans are the zonally oriented teleconnection patterns that are prominent during northern winter (Branstator 2002). These patterns consist of chains of upper

tropospheric highs and lows centered along the planetary wave guide near the core of the subtropical jet. Since these patterns extend throughout the depth of the troposphere, they have the potential to influence the extratropical oceans.

The SST anomalies driven by changes in the storm tracks and large-scale atmospheric circulation anomalies are spread throughout the surface layer of the ocean via turbulent mixing. Namias and Born (1970, 1974) were the first to note a tendency for midlatitude SST anomalies to recur from one winter to the next without persisting through the intervening summer and hypothesized that the SST anomalies reappear due to the seasonal cycle in ocean mixed layer depth (MLD). Temperature anomalies that form at the surface spread over the deep mixed layer in winter and then remain at depth when it shoals in spring. During summer, these thermal anomalies are sequestered within the seasonal thermocline (approximately 25-120 m), while surface fluxes damp the temperature anomalies within the mixed layer. When the MLD increases in autumn, the anomalies are re-entrained into the surface layer, influencing the SST. This process, termed the “reemergence mechanism” by Alexander and Deser (1995), occurs over a substantial portion of the world’s extratropical oceans (Alexander et al. 1999; Watanabe and Kimoto 2000; de Cöetlogon and Frankignoul 2003).

Upper ocean processes, including the reemergence mechanism contribute to interannual and decadal variability of the extratropical oceans. Pronounced decadal fluctuations occurred over the North Pacific during the 20th century, which Mantua et al. (1997) termed the Pacific Decadal Oscillation (PDO) based on transitions between relatively stable states of the dominant pattern of North Pacific SST anomalies. The spatial structure of the PDO resembles a horseshoe with anomalies of one sign in the central Pacific and anomalies of the opposite sign around the rim of the basin. The SST transitions were

accompanied by widespread changes in the atmosphere, ocean and marine ecosystems (e.g. Miller et al. 1994; Trenberth and Hurrell 1994; Benson and Trites 2002). The myriad of mechanisms proposed to explain extratropical decadal climate variability, including the PDO, can be classified into three broad categories: extratropical, tropically forced and those due to tropical-extratropical interactions. Extratropical mechanisms for SST variability include stochastic atmospheric fluctuations which force the ocean via surface heat fluxes and by wind driven adjustments in the ocean circulation via long baroclinic Rossby waves (Frankignoul et al. 1997; Jin 1997; Zorita and Frankignoul 1997). The latter may be especially important for decadal variability as westward propagating Rossby waves integrate wind stress forcing (Sturges and Hong 1995; Frankignoul et al. 1997) and the first baroclinic Rossby wave, which is strongly forced by the wind, takes approximately 5-8 years to cross the ocean in midlatitudes (Latif and Barnett 1994). Variability in the thermocline associated with Rossby wave dynamics influences SSTs in the vicinity of the western boundary current and its extension (Miller et al. 1998; Deser et al. 1999; Schneider and Miller 2001). If these SSTs exert a strong positive feedback on the atmospheric circulation, air-sea interaction combined with fluctuations in the extratropical ocean gyres may result in self-sustaining decadal oscillations (Latif and Barnett 1994, 1996; Miller and Schneider 2000).

Atmospheric teleconnections from the tropical Pacific can impact North Pacific SSTs either through variability in the surface forcing at decadal time scales (Trenberth 1990, Graham et al. 1994, Deser et al. 2004) or by ENSO-related forcing on interannual time scales which is subsequently integrated, or “reddened”, by the reemergence mechanism and

wind forced Rossby waves in the North Pacific (Newman et al. 2003; Schneider and Cornuelle 2005).

In the tropical-extratropical mechanisms for decadal variability, the atmospheric component is essentially the same as in the tropical forcing paradigm, but the decadal time scale is set by the ocean, either through the advection of ocean thermal anomalies from the North Pacific to the equator (Gu and Philander 1997) or by changes in the strength of the tropical-extratropical circulation (Kleeman et al. 1999; McPhaden and Zhang 2002). The equatorward flow is part of a shallow (< 500 m) overturning circulation, termed the subtropical-tropical cell (STC): subtropical water subducts into the main thermocline, upwells at the Equator, and then returns to the subtropics in the thin surface Ekman layer (e.g. Molinari et al. 2003).

Here we examine extratropical atmospheric and oceanic processes and tropical-extratropical interactions in an extended CCSM3 control simulation and compare the results to observations whenever possible. In general, we seek to understand mechanisms for the evolution of Northern Hemisphere SST anomalies, as they play a crucial role in atmosphere-ocean variability in the climate system. CCSM3 is briefly described in section 2; storm tracks and their relation to SST anomalies are examined in section 3; the relationship between clouds and atmosphere and ocean variability is examined in section 4; patterns of atmospheric and oceanic variability, including the NAO and PDO, are discussed in section 5, the upper ocean thermal structure and reemergence mechanism are examined in section 6, and thermocline variability and the upper ocean current structure are examined in sections 7 and 8, respectively. The results are briefly summarized in section 9.

2. Model description

The Community Climate System Model (CCSM), version 3, has four major components representing the atmosphere, ocean, cryosphere and land surface that are linked via a flux coupler. There have been improvements in several aspects of the model relative to its previous version, CCSM2, including new treatments of cloud processes, aerosol radiative forcing, land-atmosphere fluxes, ocean mixed-layer processes, and sea-ice dynamics (Collins et al. 2005a).

The Community Atmosphere Model (CAM3, Collins et al. 2005b), is a global atmospheric general circulation model (AGCM). The standard version of CAM3, which is used here, has 26 vertical levels and is based upon the Eulerian spectral dynamical core with triangular truncation at 31, 42, and 85 wave numbers, horizontal resolutions of approximately 3.75°, 2.8° and 1.4°, respectively. The Community Land Model (CLM, Briegleb et al. 2004) grid is identical to that of CAM3. The ocean general circulation model is an extension of the Parallel Ocean Program (POP, Danabasoglu et al., 2005) originally developed at Los Alamos National Laboratory. For resolutions of T42 and higher, POP has 40 vertical levels and a horizontal resolution of approximately 1°. The Community Sea-Ice Model (CSIM, Briegleb et al. 2004) grid is identical to POP's.

Here we focus on an extended (> 600 year) control simulation of CCSM3 at T85 resolution for the atmosphere and land and a 1° grid for ocean and sea-ice, the configuration used in the NCAR climate-change simulations. In control integrations, the CO₂ is fixed at present day values. A similar control CCSM3 simulation was performed using the T42 version of CAM3. The T42 and T85 control simulations are compared to each other and to observations on the web (Stevens et al. 2005, <http://www.cgd.ucar.edu/>

cms/stevens/master.html, where the T42 and T85 control integrations are referenced as experiments b30.004 and b30.009). The results from the T42 version are not presented here as most variables we examined were similar to those in the T85 experiment, but notable differences between the two experiments are discussed in the text. In section 8, an uncoupled POP simulation forced with observed atmospheric conditions over the period 1958-2000 is also used to study the flow within the thermocline.

3. Storm tracks and their relation to SST anomalies

We assess the atmospheric variability associated with storm tracks in CCSM3 using both a cyclone tracking algorithm and transient eddy statistics based on bandpass-filtered data to retain variability on synoptic time scales (e.g., Blackmon et al. 1977). The two provide complementary information: the former indicates the trajectories of both surface lows and highs, while the latter emphasizes the magnitude of tropospheric variability in the Pacific and Atlantic storm tracks. The cyclone tracking algorithm is similar to Murray and Simmonds (1991) and uses a descent method (Powell 1964) to determine the location of the sea level pressure (SLP) minimum (maximum for anticyclones); tracks are then formed using the long-term monthly mean 700 hPa wind field. Storm tracks are also represented by 300 hPa geopotential height variance (z'^2), which is calculated using daily data that is high pass filtered to retain fluctuations on synoptic time scales (~2-8 days). The observational data are from the European Center for Medium Range Forecasts (ECMWF) 40-year Re-Analysis (ERA-40). ERA-40 2.5° lat x 2.5° lon 6-hourly sea level pressure (SLP) and geopotential height fields have been averaged to produce daily mean fields. The data are compared to daily output from the CCSM3 T85 simulation during December-March (DJFM), where the years specified correspond to JFM of a given winter.

The average of the cyclone trajectories during boreal winter in ERA-40 (years 1958-2000) and in CCSM3 (years 501-540) are very similar over the open oceans, but ERA-40 has more storm activity over the Mediterranean and to the south of the Caspian Sea compared to the model (Fig. 1). In addition, ERA-40 indicates a local maxima in the lee of the Rocky Mountains that is much weaker and more diffuse in the model. This deficiency is slightly less marked in the T85 simulation than in the T42 simulation (not shown), suggesting that the resolution of topography may be a factor in resolving lee cyclogenesis in the model. The anticyclone tracks in CCSM3, which extend over most of the North Pacific and from Hudson Bay (65°N , 80°W) to the Kara Sea (75°N , 70°E), are strikingly similar to observations (not shown).

The influence of ENSO on storm tracks is depicted in Fig. 2, based on the composite difference in storm track density between the ten winters with the warmest and coldest SSTs in the Nino3.4 region (5°N - 5°S , 170°W - 120°W) during 1958-2000 in ERA-40 and years 501-540 in CCSM3. In the eastern Pacific, there is a meridional dipole anomaly between about 160°W - 130°W , which indicates a southward displacement of the cyclone trajectories in the storm track exit region during El Niño (warm ENSO) in both ERA-40 and CCSM3. Both the model and observations also indicate a significant decrease in storm activity to the south of the Kamchatka Peninsula in the western Pacific, but unlike observations, CCSM3 indicates a significant enhancement in storm activity over eastern Siberia. In the Atlantic, ERA-40 indicates a southward displacement of the storm track along the eastern seaboard with a marked increase in activity over the western North Atlantic, a feature that is present albeit weaker in CCSM3.

Empirical orthogonal function (EOF) analysis is used to calculate the leading modes of interannual variability of the Pacific and Atlantic storm tracks during DJFM. Regressions

of 300 hPa z^2 on the principal components (PCs) of the two leading modes of 300 hPa z^2 variability for years 101-600 of the CCSM3 control run over the Pacific (120°E-120°W, 20°N-80°N) and Atlantic (90°W-30°E, 20°N-80°N) are shown in Fig. 3, superimposed on the climatological storm tracks. EOF 1 for both the Pacific and Atlantic is an equatorward shift of the storm track exit, and EOF 2 for both basins is a strengthening of the storm track. The small regression coefficients of Atlantic 300 hPa z^2 on the leading modes of variability in the Pacific, and vice-versa, suggest that the relationship between variability in the two storm tracks is quite weak.

The same EOF analysis is performed on the DJFM storm tracks in ERA-40 for the period 1958-2000. While Harnik and Chang (2003) show that the NCEP-NCAR reanalysis underestimates upper-level storm track strength relative to radiosonde observations prior to the late 1970s, the ERA-40 storm tracks are stronger than NCEP-NCAR reanalysis storm tracks for the period 1958-1978 (not shown), and including the years before 1979 has little effect on the EOF analysis aside from a reordering of the first 3 Atlantic EOFs. For both the Pacific and Atlantic in ERA-40, EOF 1 is a strengthening of the storm track and EOF 2 is an equatorward shift of the storm track exit; regressions of 300 hPa z^2 on the corresponding PCs are shown in Fig. 4. Differences between CCSM3 and ERA-40 modes of storm track variability appear related to biases in CCSM3 climatological storm tracks, which are similar to those found in CAM3 (Hurrell et al. 2005).

The southward shift in the path of the individual cyclones during El Niño events shown in Fig. 2, suggests that ENSO should impact the leading modes of storm track variability in the upper troposphere. While the PC corresponding to an equatorward shift of the CCSM3 Pacific storm track exit has a correlation of 0.42 with the time series of Niño3.4

SST anomalies, which is significant at the 99% level, the relationship between ERA-40 Pacific storm track PCs and ENSO is more complex. Only PC 1 (strengthening) has a significant correlation (0.44) with Nino3.4 over the entire period 1958-2000, while PC 2 (equatorward shift) has an insignificant correlation of 0.23. When the first half (1958-1978) and second half (1980-2000) of the ERA-40 time series are considered separately, only PC 1 has a significant correlation (0.70) during the first half, while only PC2 has a significant correlation (0.50) during the second half. Regressions of 2-8 day 300 hPa z'^2 on the Nino3.4 time series (not shown) also show a strengthening of the Pacific storm track for 1958-1978, an equatorward shift of the Pacific storm track exit for 1980-2000, and a combination of the two for 1958-2000. Because the SST anomalies associated with ENSO are narrower in CCSM3 than in observations (Deser et al. 2005), the CCSM3 storm track response to ENSO may be more like 1980-2000, when the observed ENSO SST anomalies were narrower than during 1958-1978; the short record of storm tracks from ERA-40 may also affect the significance of the observed storm track-ENSO relationships.

To investigate whether these modes of interannual storm track variability are coupled to extratropical SST and land temperatures, surface temperatures in CCSM3 and ERA-40 are regressed on the corresponding storm track PCs (color shading in Figs. 5 and 6). All of the modes of storm track variability except for the strengthening of the Atlantic storm track in CCSM3 are accompanied by patterns of SST that have the potential to reinforce the storm track pattern, i.e. an increase in the meridional SST gradient equatorward of where the storm track increases in strength, as the storm track at a particular latitude is most influenced by the surface temperature gradient 5° to 10° equatorward of its latitude due to the poleward tilt of baroclinic waves with height (Yin and Battisti 2004). While SST

changes little with a strengthening of the Atlantic storm track in CCSM3, the surface temperature gradient is enhanced upstream over North America.

Regressions of 1000 hPa zonal wind on the PCs of storm track variability (contours in Figs. 5 and 6) show that low-level winds tend to be more westerly where SSTs are cooler over the Pacific, implying that the SST anomalies are driven by winds either through surface heat fluxes or Ekman transport across the meridional SST gradient. This relationship also appears to hold in the Atlantic, although in CCSM3 the stronger zonal winds near the east coast of the U.S. appear to be offset by another process, probably warm southerly advection by either anomalous southerly winds or the Gulf Stream. In turn, the changes in low-level zonal winds are consistent with the changes in poleward momentum flux that are expected to accompany the shifts in the storm tracks.

The relationship between the storm tracks and SST in June-August (JJA) is somewhat less clear. The first EOF of JJA 2-8 day 300 hPa z'^2 is a weakening and equatorward shift of the storm track in both the Pacific and Atlantic in CCSM3 and ERA-40 (black contours in Fig. 7), although the patterns are somewhat stronger and more extensive in the model. The poleward shift of CCSM3 storm track EOFs relative to ERA-40 reflects the poleward shift of the JJA mean storm tracks relative to ERA-40 (not shown), which is also found in CAM3 (Hurrell et al. 2005). The SST anomalies regressed on the corresponding storm track PCs (color shading in Fig. 7) shift the strongest meridional SST gradient equatorward, and thus may reinforce the storm track anomalies. Lag regression analysis shows that the SST anomalies are largest when they lag the storm track anomalies by about 1 month in both summer and winter (not shown), implying that the atmosphere is forcing the SST anomalies, but the link between the storm track and the SST forcing is not clear in JJA. Although the 1000

hPa zonal wind anomalies regressed on the storm track PCs (not shown) line up reasonably well with the SST anomalies in the Atlantic, in the Pacific the SST and zonal wind anomalies are in approximate meridional quadrature and further analysis is required to explain the forcing of the SST anomalies that accompany the dominant pattern of JJA storm track variability over the North Pacific. However, it is encouraging that the relationship between storm tracks and SST is similar between CCSM3 and observations in both summer and winter.

4. Summertime cloud-SST variability

Shortwave radiative forcing by clouds is an important factor that influences extratropical SSTs in summer (e.g. Norris et al. 1998); regressions of CCSM3 and observed upper level cloud anomalies on JJA storm track PCs (not shown) have considerable overlap with the Pacific SST anomalies, suggesting that shifts in upper-level clouds could also be forcing Pacific SST in summer. Meridional advection ahead of and behind cold fronts in extratropical cyclones strongly influences low-level clouds via interaction with the underlying ocean: poleward advection of warm subtropical air over colder water enhances stratification leading to saturation of the boundary layer and the formation of fog or shallow stratus (Norris 1998; Norris and Klein 2000; Norris and Iacobellis 2004), while equatorward advection of midlatitude cold-sector stratocumulus over warmer water leads to decoupling of the cloud and subcloud layers and subsequent stratocumulus breakup (e.g., Wyant et al. 1997). As a result, the climatological low-to-mid level cloud fraction is high (low) north (south) of $\sim 40^{\circ}\text{N}$ over the northern oceans during boreal summer, which is simulated reasonably well in CCSM3 (Stevens et al. 2005).

The correlation between low-level cloud amount and SST over the midlatitude North Pacific and North Atlantic during JJA in observations and CCSM3 are shown in Fig. 7. Individual ship low-level cloud cover reports collected in the Extended Edited Cloud Report Archive (EECRA, Hahn and Warren 1999) and monthly SST anomalies from Kaplan et al. (2000) were averaged over JJA and within $5^{\circ} \times 10^{\circ}$ grid boxes during 1958-97. Corresponding monthly CCSM3 low-level cloud fraction and SST values from twelve sequential 40-year segments (years 100-579) were also averaged over JJA and linearly interpolated to the observed grid. The availability of twelve realizations enables an assessment of the likelihood that differences between CCSM3 and observed correlations are not merely due to chance. CCSM3 reproduces the observed bands of large negative cloud-SST correlation across the North Pacific and North Atlantic between 30°N - 50°N as well as areas of negative correlation over eastern subtropical oceans, near the southeastern U.S., and near the British Isles (Fig. 8). These negative correlations indicate that low-level clouds act as a positive feedback on SST anomalies in CCSM3, as occurs in nature (e.g., Norris et al. 1998; Frankignoul and Kestenare 2002; Park et al. 2004). However, the cloud-SST correlations are more negative in CCSM3. Sampling uncertainty may be a contributing factor to the weaker observed correlations, but there may also be an unrealistic sensitivity between low-level cloud fraction and SST in CCSM3. The unrealistic negative correlation exhibited by CCSM3 in the western subtropical North Pacific probably has little impact on the simulation because the magnitude of interannual low-level cloud anomalies in this region is very small (not shown).

Despite the general resemblance of observed and CCSM3 low-level cloud-SST correlation patterns, not all cloud processes are correctly represented in CCSM3. The correlation between low-level cloud amount and near-surface meridional wind component

obtained from monthly values of National Centers for Environmental Prediction (NCEP) reanalysis 1000 hPa wind (Kalnay et al. 1996) and CCSM3 lowest layer wind are shown in Fig. 9. Although CCSM3 reproduces the observed negative correlation between low-level cloud amount and meridional wind over eastern subtropical oceans, it exhibits positive rather than negative correlations over the midlatitude North Pacific and North Atlantic. The primary cause of the erroneous correlations in CCSM3 is that the large-scale cloud fraction parameterization underproduces midlatitude stratocumulus when there is southward flow, a problem common to other AGCMs (e.g., Tselioudis and Jakob 2002), while overproducing stratus clouds around 40°N when warm air is advected over cold water.

5. Atmospheric and SST Patterns of Variability

Much of the variability in the extratropical atmosphere and ocean occurs in coherent large-scale patterns. In this section, we examine the patterns of variability in the Pacific and Atlantic sectors and their relationship to local air-sea interaction and tropical forcing.

a. Waveguide patterns

Anomalies associated with the atmospheric waveguide, consisting of alternating highs and lows near the core of the subtropical jet during winter, have been found in an earlier investigation of two AGCMs and nature (Branstator 2002). They are of interest to our study because they have the potential to initiate North Pacific large scale air-sea interaction from remote midlatitude locations. Here we employ one point correlation plots of monthly anomaly fields to determine whether these patterns are also present in the CCSM3 control integration and to see whether they interact with the extratropical North Pacific Ocean.

Prior to computing correlation patterns for a field, remote tropical influences are removed using a linear regression relationship between interannual variations in grid point values of that field and concurrent interannual variations in the first ten principal components of Southern Hemisphere monthly mean 300 hPa stream function. This filter is based on the notion that Northern Hemisphere variability associated with Southern Hemisphere variability is instigated by tropical SST anomalies.¹

To verify that the waveguide teleconnection patterns occur in CCSM3, we produced one-point correlation plots of 300 hPa stream function for January means during years 100-599 of the CCSM3 T85 control integration. Fig. 10 shows the one point correlation chart for a master point at 127.5°E, 33°N. This map is qualitatively similar to many such charts with master points in the vicinity of the Asian subtropical jet and shows that CCSM3 does have zonally oriented patterns that extend across the expanse of the Northern Hemisphere like those found by Branstator (2002). Consistent with the linear model solution of Rossby wave propagation (Branstator 2002), the phase of this pattern shifts longitudinally if one moves the longitude of the master point and its zonal extent is also affected by such shifts. For example, with a master point at 90°E, 29°N the atmospheric anomalies are confined to the western half of the North Pacific (not shown) rather than the circumpolar pattern the anomalies seen in Fig. 10.

Having established that waveguide patterns exist in CCSM3, we seek to determine whether they interact with the underlying ocean. One indication that there is such an interaction comes from calculating correlations between 300 hPa January stream function

1. A more conventional filter based on the leading principal components of tropical SST variability gave qualitatively similar results, though it appeared to remove midlatitude initiated relationships with the tropics, an undesirable characteristic for our study.

at the master point used in Fig. 10 and simultaneous variations in SLP (Fig. 11a) and surface temperature (Fig. 11b). These correlations indicate that the upper tropospheric circumglobal pattern is strongly connected to surface atmospheric and oceanic variations, with the linkages being especially strong over the North Pacific. In particular, SLP anomalies are nearly collocated with height anomalies at 30°N, 125°E and 35°N, 170°W, while the associated surface temperature anomalies are located where the SLP gradient and thus the winds and temperature advection are strong. (All of the features discussed here occur in both the first and second half of the GCM record and thus appear to be robust.)

To investigate whether this association between the waveguide pattern and SST anomalies is initiated in the atmosphere or ocean, we calculate the correlations between the waveguide pattern and thermal fluxes (sensible heat, latent heat, net longwave radiation and net shortwave radiation). There are substantial correlations in some regions of the North Pacific for all of these quantities, but regression analyses indicate that the magnitude of the radiation flux anomalies are weak compared to the heat fluxes (not shown). The latent and sensible heat flux correlations (Fig. 11c-d) indicate that where SST is above normal there is above average heat flux from atmosphere to ocean, and where ocean SST is below normal there is below normal heat flux from atmosphere to ocean. Thus, the fluxes are generally consistent with the atmosphere driving the ocean throughout the North Pacific. The properties we have noted for the waveguide pattern in Fig. 11 are true for all other patterns associated with the subtropical jet that we have examined; they all influence the North Pacific through heat fluxes, though the geographical reach of the fluxes depends on the longitudinal phase of the circulation anomalies.

Since in CCSM3 the interaction of the circumglobal waveguide pattern with the ocean is one of the atmosphere forcing the ocean, given the ocean's large thermal inertia one

would expect to find larger correlations of this atmospheric pattern with lagged rather than simultaneous SST. Fig. 12a shows February surface temperature correlated with January 300 hPa streamfunction at 127.5°E, 33°N. All of the main midlatitude North Pacific features are indeed stronger than they were for simultaneous correlations (Fig. 11b). One month lagged correlation plots of other quantities including 300 hPa streamfunction and surface heat fluxes (not shown) indicate that the atmospheric processes that produced the North Pacific SST anomalies in January have almost disappeared by February. Thus it is not surprising that two month lagged surface temperature correlations (Fig. 12b) are weaker than their one month lagged counterparts since the atmospheric anomalies are no longer there to help maintain them.

Spurred by studies like that of Barsugli and Battisti (1998), a commonly asked question is whether the atmospheric-induced midlatitude SST anomalies feed back onto midlatitude atmospheric anomalies, and if so whether the feed back is positive. For the waveguide initiated North Pacific anomalies, we do see a positive feedback in the sense that lagged midlatitude temperatures in the lowest atmospheric level have substantial persistence with a structure that matches underlying lagged SST anomalies (not shown). Since the upper tropospheric waveguide patterns in the lagged months are nearly gone, these near surface temperatures are almost certainly being supported by the ocean anomalies. However, the negligible amplitudes of the lagged upper tropospheric anomalies indicate that the feedback does not reach these levels in any substantial way.

b. North Pacific variability

The low-frequency extratropical atmospheric circulation is generally described in terms of “teleconnection patterns” (e.g. Wallace and Gutzler 1981), which are spatially

stationary structures whose amplitudes fluctuate in time. Typically these patterns are identified using techniques that assume linear behavior so that events in which the pattern has one sign are just as important as events of the opposite sign in representing observed behavior. Atmospheric variability can also be examined through a non-linear analysis known as cluster decomposition (Andelberg 1973). This method, based on classification techniques, seeks preferred and/or recurrent quasi-stationary atmospheric patterns or “regimes” that are spatially well defined (but without symmetry constraints) and limited in number. While regime analyses can provide useful information on the pattern and polarity of climate anomalies, their significance in identifying non-normal behavior is uncertain due to the limited number of observations (e.g. Stephenson et al. 2004). Thus, consistency between regimes identified in observations and long climate model simulations can provide additional evidence of their validity.

Climate regimes over the North Pacific (130°E - 80°W , 20°N - 80°N) are first determined in individual winter months (December-March) during years 100-599 of the CCSM3 control simulation. We used the k -mean partitioning scheme (Michelangeli et al. 1995) and found $k=4$ to be the optimal number of statistically significant regimes to be retained. Composite maps of SLP anomalies for the sets of months belonging to each regime are shown in Fig. 13a-d. The first two regimes are reminiscent of the Pacific North American (PNA+) pattern and its opposite (PNA-) (Wallace and Gutzler 1981). Spatial asymmetries between the two phases are found in the eastward extension of the North Pacific anomalous pressure centers and in the related southward penetration of the higher latitude core over the North American continent. Regimes 3 and 4 form another pair with an anomaly center near Alaska. The strong high in the former is often associated with blocking conditions, while the deepening and eastward shift of the Aleutian Low in the

latter could be viewed as the regional signature of the “Tropical North Hemisphere” (TNH) mode (Barnston and Livezey 1987; Straus and Shukla 2002). Regime 3 and 4 will be henceforth referred to as ALE+ and ALE- respectively. Counterparts can be found in observations as identified by Robertson and Ghil (1999) or Michelangeli et al. (1995), although decompositions were conducted from low-pass filtered daily maps instead of monthly means. PNA+ and PNA- are equally excited (26% occurrences) and represent about half of the total sample, while ALE- occurs more often (29%) than ALE+ (19%) in the model.

It is well known that the North Pacific extratropical atmosphere is affected by anomalous SST conditions in the entire Pacific basin. Composite DJFM average surface temperature (TS) anomalies are constructed when at least three of four months are occupied by a given regime (see Cassou et al. 2004b for further details). All regimes are associated with SST anomalies in both the tropical and North Pacific that are the hallmark of ENSO (Fig. 13e-h). PNA+ (PNA-) is linked to the warm (cold) phase of ENSO and to North Pacific SST anomalies associated with the atmospheric bridge mode characterized by warm (cold) oceanic conditions along the North American west coast and colder (warmer) SSTs in the central basin. Anomalous TS over the continents show contrasts between the sub-polar areas of North America and Eurasia. The temperature patterns are fairly symmetrical between the PNA regimes and suggest a strong correlation between the PNA mode simulated in the model and the Northern Annular Mode (NAM) described in Thompson and Wallace (1998). Compared to observations, such a relationship appears overestimated (not shown) and has a strong impact on the North Atlantic atmospheric dynamics (Cassou and Terray 2001). Both ALE regimes are clearly linked to ENSO: El

Niño episodes are associated with a deepening of the Aleutian Low (ALE-), while blocking episodes occur more often during La Niña.

To better illustrate the forcing role of ENSO, relative changes of occurrence for each regime are computed depending on its phase and presented in Table 1. El Niño events clearly favor ALE- while strongly reducing the excitation of the PNA- regime. Although not significant, warm events tend to excite the PNA+ (ALE+) regimes more (less) frequently. La Niña changes the frequency of both PNA phases about equally, with a strong increase in the PNA- and decrease in the PNA+ regimes. La Niña's influence on the ALE regimes is rather limited. Our findings are consistent with studies showing significant non-linearity of the extratropical response to tropical forcing (Lin and Derome 2004); in particular, CCSM3 is able to correctly simulate the dominant influence of cold events on the PNA teleconnection pattern, while warm events also influence the ALE regime that is linked to the TNH pattern. Such an asymmetry results in an eastward shift of the North Pacific negative pressure anomaly during warm events compared to cold events, as found in other models (Lin and Derome 2004) and observations (Hoerling et al. 1997; DeWeaver and Nigam 2002).

The dominant pattern of SST variability in the North Pacific, the PDO, is defined using the leading EOF of monthly SST anomalies north of 20°N. The wintertime (November-March) average of the PDO index, the PC associated with EOF 1, is shown for a 100-year period from both observations and the model in Fig. 14a-b. The observed values are based on historically reconstructed SSTs for the period 1900-1999 (Mantua et al. 1997); the model results are from years 500-599 in the CCSM3 control integration. While a direct correspondence is not expected between the model and nature, both show pronounced

decadal variability, with periods of 10 years or more where the PDO index is predominantly of one sign.

Relative changes in the frequency of occurrence of the North Pacific regimes (Fig. 13) associated with PDO are significant but much weaker than for ENSO (Table 1). The positive phase of the PDO, with cold water in the central North Pacific, is associated with the positive (negative) phase of the PNA (ALE) pattern, while only the PNA- regime is enhanced during the negative phase of the PDO.

We explore the spatial structure of the PDO by correlating it with the concurrent near surface air temperatures during winter (Fig. 14c-d). Over the North Pacific, the simulated and observed PDO temperature patterns are very similar, as both have negative correlations between about 35°N-50°N in the central to western Pacific and positive correlations along the coast of North America that extend southwestward toward Hawaii.² The correlations in both the model and observations also suggest a downstream wave train with centers of opposite sign over Alaska/western Canada and the southeast United States (also see Stevens et al. 2005). However, CCSM3 is markedly different from nature in terms of the PDO's connection to the tropics: strong positive correlations across most of the tropical Pacific in observations are absent in the model.

c. North Atlantic variability

The four SLP regimes over the North Atlantic (20°N-80°N, 80°W-30°E), shown in Fig. 15a-d, are obtained following the same cluster analysis approach as used in the Pacific.

2. A similar spatial structure for the PDO in both observations and the model is obtained from EOF 1 of the North Pacific SST anomalies, but the model has excessive amplitude to the east of Japan, which is likely due to the greater than observed variance in that region.

Regimes 1 and 2 capture the positive and negative phase of the NAO. The third cluster displays a strong anticyclonic ridge off western Europe (ATL⁺) while the fourth is dominated by a trough covering the entire northern portion of the domain (ATL⁻). With the exception of regime 4, all have counterparts in nature, although there are differences in the structure of the regimes relative to observations (Cassou et al. 2004b). Although the model is able to simulate the eastward shift of the Azores High for NAO⁺ towards Europe, as part of NAO variability, the Icelandic low extends too far to the east, leading to stronger than observed zonal flows. The high in the ATL⁺ pattern is displaced to the northeast and does not include the wave pattern from the subtropics to the Baltic Sea as found in observations. The latter is likely related to biases in the mean climate: the Icelandic Low is stronger and displaced to the southeast in CCSM3 relative to observations. The NAO and ATL⁻ regimes are very similar in CCSM3 and CAM3 (not shown), which suggests that the biases in the North Atlantic regimes are mainly due to atmospheric processes and not air-sea coupling.

As in nature, surface temperature anomalies associated with the NAO regimes have a quadrupole pattern over the continents adjacent to the North Atlantic Ocean, with anomalies of opposite sign over the northern and southern portions of North America and over northern Europe and North Africa (Figs. 15e-h). Over the ocean, SST anomalies bear some resemblance to the North Atlantic tripole, especially for NAO⁻. The significant North Pacific SST signal associated with the NAO⁺ regime suggests a connection between the two basins through the NAM mode, as diagnosed earlier from the Pacific regimes. The ATL⁺ (ATL⁻) is associated with downstream warm (cold) SST anomalies that are consistent with the atmosphere forcing the land or ocean. The ATL⁺ and ATL⁻ regimes are weakly linked to El Niño and La Niña events, respectively, in CCSM3 contrary to the

connection found in observations (c.f. Cassou et al. 2004). This bias is not found in CAM3 simulations and could be explained by air-sea coupling that overestimates the see-saw between the Icelandic and Aleutian Lows (not shown).

6. Upper Ocean Temperature and Mixed Layer Depth

The results from sections 3-5 suggest that extratropical atmospheric variability, whether generated by internal dynamics or in response to tropical SST anomalies can force extratropical SST variability. These midlatitude SST anomalies penetrate into the ocean through physical ocean processes, such as vertical mixing and advection, and return to the surface at another time and/or location. Furthermore, ocean processes not only modulate thermal anomalies but can generate extratropical SST anomalies, via adjustments in the thermocline. In the subsequent sections we explore the role of vertical mixing, thermocline adjustment and advection on the climate of CCSM3.

The evolution of the ocean anomalies, whether forced by the atmosphere or generated by ocean dynamics, are strongly influenced by the climatology of the upper ocean, including the vertical structure of temperature, salinity, currents and MLD, which vary with season and location. The mean seasonal cycle of temperature and MLD from observations and CCSM3 are presented in Fig. 16 for regions in the central North Pacific (35°N - 45°N , 165°E - 175°W) and North Atlantic (50°N - 60°N , 20°W - 40°W). The observed temperature and MLD values are obtained from the World Ocean Atlas (Levitus et al. 1998) and Monterey and Levitus (1997), respectively. Both the observed and simulated MLD values are based on density criteria, but the former is from the difference with the surface density while the latter is the depth of the maximum vertical gradient that is nearest the surface.

The model reproduces the general structure of the seasonal cycle with maximum (minimum) temperatures at the surface in September (March) and a strong seasonal thermocline, in which the temperature decreases rapidly with depth beneath the mixed layer during summer. The temperatures throughout the upper ocean are too cold (also see Large and Danabasoglu 2005), while the wintertime MLD is underestimated, particularly in the Atlantic. A broader comparison of MLD between the model and observations indicates that the winter MLDs are over (under) estimated over much of the North Pacific (Atlantic), while the summer MLDs are well simulated in both basins (not shown).

The central North Pacific and Atlantic are candidate regions for the reemergence mechanism as they undergo a large seasonal cycle in MLD, are remote from regions of subduction and strong eddy activity, and are similar to areas where observations indicate that SST anomalies recur from one winter to the next (Alexander et al. 1999; Timlin et al. 2002). Regressions of CCSM3 temperature anomalies as a function of month and depth on temperature anomalies averaged over the three upper model layers (0-30 m) during February-April (FMA) are shown for these two regions in Fig. 17. The regressions are computed at each model point and then averaged over the respective regions. In the Pacific, the anomalies extend over the depth of the mixed layer (120-140 m) in winter, and decrease only slightly in amplitude between 50-100 m through September but are reduced by more than 50% in the surface layer over the same period. A portion of the signal, indicated by regression values of $> 0.5^{\circ}\text{C}$, returns to the surface in the subsequent December-March. In the North Atlantic, where the wintertime MLD exceeds 300 m (Fig. 16), the reemergence signal extends over greater depths and the values returning to the surface in the winter are relatively high ($>0.8^{\circ}\text{C}$) compared with the Pacific. The difference between the reemergence

mechanism in the two basins is consistent with the findings of Deser et al. (2003), which showed that the deeper the winter MLD, the further the anomalies penetrate into the ocean, which increases the effective thermal inertia of the system and enhances the winter-to-winter persistence of SST anomalies.

A cross-basin view of the reemergence process is obtained by correlating temperature anomalies in the summer seasonal thermocline, 65-85 m depth in August-September, with SST anomalies from the previous January through the following April at each model grid point and then averaging the correlation coefficients (r values) between 42°N and 52°N across the Pacific and Atlantic oceans (Fig. 18). Evidence for the reemergence mechanism is clearly seen across much of the North Pacific: relatively high r values in the previous and following winter and low values in the intervening summer. In the Atlantic, the correlations suggest that reemergence occurs between 0° - 20°W and 30°W - 50°W . The absence of recurring SST anomalies between 50°E and the North American coast in CCSM3 is consistent with the observational analyses of Timlin et al. (2002), who showed that the reemergence process did not occur in this region since the summer-to-winter difference in MLD was less than 50 m.

7. Extratropical thermocline variability and its relation to SST and air-sea interaction

SST and other surface ocean variables tend to have spatial and temporal scales commensurate with the large-scale atmospheric forcing that predominantly drives them. In contrast, thermocline variations are insulated from direct turbulent and diabatic contact with the atmosphere and are thus primarily driven by ocean dynamics. We examine the evolution of the depth of the $26.8 \sigma_{\theta}$ ($=1026.8 \text{ kg/m}^3$) isopycnal to study the thermocline

variability and its relation to the surface variables in the North Pacific during years 350-599 in the CCSM3 experiment. In the Pacific, the $26.8 \sigma_\theta$ isopycnal is generally located at the bottom of the main thermocline in both the CCSM3 simulation and observations (Roden 1998). The first EOF of the annual mean depth of $26.8 \sigma_\theta$ north of 20°N in the Pacific has anomalies of one sign between approximately 30°N - 50°N with maximum amplitude in the Kuroshio-Oyashio Extension region centered along 40°N in the western Pacific (Fig. 19a). Fluctuations associated with a one standard deviation change in the corresponding time series reach a maximum of ~ 50 m in the vicinity of 40°N , 150°E . The Kuroshio-Oyashio Extension is where the maximum meridional gradient in the climatological mean depth of the $26.8 \sigma_\theta$ surface is found, and thus, EOF 1 is likely associated with a north-south shift of the axis of the Kuroshio-Oyashio extension. The PC associated with EOF 1 has a spectral peak at around ~ 9 years, which is significantly different from a red noise spectrum at the 99% confidence level (Fig. 19c). Lag regression of the $26.8 \sigma_\theta$ isopycnal depth onto PC 1 (not shown) indicates that this pattern originates from the eastern subpolar region around 45°N , 160°W , and slowly expands westward over the five years prior to when EOF 1 was computed. This eastern subpolar region coincides with the location of the maximum in the first EOF pattern of the wind stress curl. The decadal time scale is also consistent with previous studies on the gyre-scale circulation changes in the North Pacific (Miller et al. 1998; Deser et al. 1999). EOF 2 has a wave-like pattern around the subpolar gyre north of 40°N (Fig. 19b). The associated PC has a spectral peak at around ~ 16 years that is significant at the 99% confidence level (Fig. 19c). In CCSM2 control experiment, a predecessor of this simulation, a pattern very similar to EOF 2 in both time scale and spatial structure clearly demonstrated counter-clockwise propagation around the subpolar

gyre. However, propagation associated with the EOF 2 pattern was not readily apparent in CCSM3.

EOFs of DJFM SST anomalies between 20°S and 60°N in the Pacific indicate that ENSO and a North Pacific mode are the first and second leading patterns of variability (Fig. 20), consistent with the observational analysis of Deser and Blackmon (1995). EOF 1 has maximum loading in the central and eastern tropical Pacific and a secondary maximum in the central North Pacific. The corresponding PC also has a strong spectral peak at around the ENSO period and a secondary peak at ~20 years (not shown). EOF 2 has very little expression in the tropics. PC 2 of SST and PC 1 of the depth of the 26.8 σ_θ surface are correlated ($r=0.39$, significant at 99% level), when the latter leads by 2 years.

In the Kuroshio-Oyashio extension region (35°N-45°N, 140°E-180°), the SSTs are related to the surface heat flux and wind stress curl as well as the thermocline depth (Fig. 21). The local correlation between SST and thermocline depth anomalies is 0.69, while the correlation between the SST and the upward net surface heat flux (wind stress curl) anomaly is 0.56 (0.34), when the SST anomaly leads by one year. These values are all significant at the 99% level and increase to 0.71, 0.72, and 0.44, respectively, when the time series are low-pass filtered for periods longer than 5 years. Therefore, in the Kuroshio-Oyashio Extension region, a deeper than normal thermocline causes a warm SST anomaly, which is damped by surface heat flux anomalies out of the ocean and induces a local atmospheric response including cyclonic wind stress curl.

8. Tropical-Extratropical Ocean Circulation

Observational studies have delineated the pathways of the flow from the subduction regions in the subtropics to the equator. In the Pacific, Johnson and McPhaden (1999) and McPhaden and Zhang (2002) have shown that the presence of the Intertropical Convergence Zone (ITCZ) in the northern Tropics (7° - 10° N) creates a “potential vorticity (PV) barrier” for the equatorward flow, which is absent in the Southern Hemisphere. As a result, the interior (i.e. away from the western boundary) flow from the northern subtropics follows a much more complex route than the equatorward flow from the Southern Hemisphere. The ocean component of CCSM3, driven by observed surface forcing over the period 1958-2000 (hereafter POP simulation) yields a PV field (Fig. 22a) that is very similar to that computed from observations (c.f. Fig. 2c of Johnson and McPhaden 1999, and Fig. 1b of McPhaden and Zhang 2002), although the PV ridge in the 7° N- 10° N band is somewhat weaker in the POP simulation. Fig. 22a shows the PV on the $25\sigma_{\theta}$ isopycnal, a density surface that lies within the core of the equatorial thermocline. In the northern hemisphere, the flow is mainly zonal in the 7° N- 10° N band, and feeds the western boundary current, while equatorward flow is confined west of $\sim 140^{\circ}$ E.

The potential vorticity field on the $25\sigma_{\theta}$ isopycnal in the Pacific from the CCSM3 simulation is shown in Fig. 22b. The PV barrier in the Northern Hemisphere is somewhat stronger than in the POP simulation, and extends further west. The main difference between PV in CCSM3 and POP (as well as observations) is a second area of large PV values in the western tropical South Pacific (150° E- 180°), associated with the erroneous precipitation maximum located across the Pacific at $\sim 8^{\circ}$ S in CCSM3 (Deser et al. 2005; Large and Danabasoglu 2005) and most other coupled GCMs. This southern PV barrier alters the flow pattern with respect to the POP simulation. Around 10° S, the isopycnal flow

in CCSM3 is more zonal, flowing westward and then northward around the western side of the PV maximum. Thus, pathways connecting the subtropical Pacific to the equator exist in CCSM3, but in the Southern Hemisphere they are not as direct as found in observations and in the POP hindcast.

In the Atlantic Ocean most of the water reaching the equator via the subtropical cell (STC) originates in the Southern Hemisphere, although interior and western boundary pathways are found in both hemispheres (e.g. Hazeleger et al. 2003; Zhang et al. 2003; Molinari et al. 2003). Lagrangian trajectories are computed on the $25.4\sigma_\theta$ isopycnal surface, which is located within the tropical thermocline and intersects the equator near the core of the equatorial undercurrent. Trajectories of “floats” released where the $25.4\sigma_\theta$ outcrops are shown at one year intervals in Fig. 23 for the POP and CCSM3 simulations; a similar observationally-based analysis is presented by Zhang et al. (2003, Fig. 5). Like observations, the broad structure of the flow in POP and CCSM3 is cyclonic on either side of the equator: clockwise (counterclockwise) in the Southern (Northern) Hemisphere. However, there are notable differences in the structure and in some locations the speed of the flow. In CCSM3, only water from the Southern Hemisphere reaches the equator, predominantly through the western boundary current, while in the POP simulation and observations there are also pathways to the equator from the Northern Hemisphere and within the interior of the South Atlantic Ocean. Trajectories on the $24.5\sigma_\theta$ and $26.0\sigma_\theta$ isopycnal surfaces (not shown) suggest that the northern pathway to the equator is absent throughout the thermocline in CCSM3. As in the Pacific, the biases in the circulation are consistent with excessive PV maxima that extend across the subtropics of both hemispheres (not shown). The current speed, as indicated by the distance between

triangles, is similar in the two integrations, except to the west of $\sim 20^\circ\text{W}$ in the Southern Hemisphere, where the flow appears to be faster in CCSM3.

The CCSM3 simulation also contains a clockwise circulation in the southeast portion of the basin that is not found in the POP simulation. While observations suggest that a domed cyclonic circulation, termed the Angola gyre, exists in this location, the density level and strength of the circulation are inaccurate in CCSM3 due to biases in the coupled atmosphere-ocean system off the coast of southern Africa (see Large and Danabasoglu 2005).

9. Discussion and Conclusions

In this study we have explored processes that influence extratropical climate variability in CCSM3 with a focus on coupled atmosphere-ocean interaction. In both nature and CCSM3, atmospheric processes, including storm tracks, clouds and climate regimes, influence large-scale atmospheric patterns and the underlying SSTs, while oceanic processes, such as the reemergence mechanism, subduction and flow within the thermocline affect the temporal and spatial distribution of these thermal anomalies and generate SST anomalies in their own right.

The mean storm track in winter is fairly well simulated by CCSM3, although the model underestimates the number of cyclones over the Mediterranean and in the lee of the Rockies. The leading modes of interannual storm track variability in CCSM3 and their relationships to SST anomalies are similar to observations as well. In response to tropical SST anomalies, the North Pacific storm track exit region shifts south during El Niño relative to La Niña events in both the model and observations. In addition, most of the leading modes

of interannual storm track variability in both CCSM3 and ERA-40 are accompanied by changes in midlatitude SST that may reinforce the storm track anomalies. If the atmospheric anomalies that accompany the modes of storm track variability also reinforce the SST anomalies, as suggested by the lag of the peak SST anomalies, this feedback loop between the storm tracks and underlying SSTs will tend to make anomalies in both persist. Such coupled ocean-storm track modes of variability would then be more likely to last for an entire season and have larger interannual variability. While more analysis is required to explain the forcing of SST anomalies by the storm tracks, especially in summer, the long record and complete sampling of atmospheric and oceanic variables provided by CCSM3 provides a useful framework for investigating the coupling between storm tracks and the upper ocean. The similar storm track-SST relationships in CCSM3 and in observations suggest that the processes involved in the coupling of storm tracks and SST in CCSM3 are likely to be important in nature as well.

During summer, positive correlations between SST and low-cloud anomalies over the Northern Hemisphere oceans are reproduced by the model. However, there are biases in the relationship between clouds and other meteorological variables, including the near surface meridional wind. Norris and Weaver (2001) found that these errors resulted from an unrealistic response in the low-level cloud amount to the near surface atmospheric circulation in CCM3, a predecessor of CAM3, and thus could influence cloud-climate feedbacks, and the atmospheric sensitivity to global warming.

CCSM3 realistically simulates several aspects of the large-scale atmospheric variability during winter. The model accurately represents the circulation anomalies associated with the wave guide induced by the jet stream, the PNA pattern, and fluctuations associated

with the Aleutian Low (ALE regime). These anomalies respond to SST anomalies in the tropical Pacific and drive SST anomalies in the North Pacific. The response to ENSO-related SSTs is nonlinear; regime analysis indicates that El Niño has a greater impact on the ALE regime, than La Niña, while La Niña has a much greater impact on the PNA pattern. The simulation of regimes in CCSM3 is less like observations in the Atlantic sector: both phases of the NAO extend too far east, as does the influence of the ATL+ regime, while the ATL- regime does not have a counterpart in observations. Similarities between the model and observed regimes, is generally seen over the Pacific, adds credence to their existence, while model-data differences may result from model error and/or from insufficient data to determine if a given regime is significant in nature.

Extratropical ocean processes in CCSM3 clearly influence upper ocean variability, including the temporal and spatial structure of SST anomalies. As in observations, surface temperature anomalies tend to recur from one winter to the next over portions of the North Pacific and Atlantic Oceans due to the persistence of these thermal anomalies beneath the mixed layer in summer. In the Kuroshio-Oyashio Extension region, fluctuations in the thermocline, driven by remote wind stress curl anomalies, influence SST, and thereby create upward surface heat flux anomalies. The local atmospheric response to these SST/surface flux anomalies could be a key element of coupled extratropical ocean-atmosphere variability, though the relationship of the local response to the basin-scale needs to be examined further.

Perhaps the greatest deficiency in the model's simulation of midlatitude climate variability is its unrealistic representation of tropical-extratropical interactions in both the atmosphere and ocean. For example, while the model obtains the basic structure of the

PDO, the leading pattern of North Pacific SST variability, the strong correlation between the PDO and SSTs in the tropical Pacific found in nature is absent in CCSM3. Since these findings are based on *concurrent* correlations, they suggest that oceanic forcing associated with atmospheric teleconnections from the tropics, a relatively rapid process, is substantially weaker than observed. The interior pathways connecting the subtropics to the equator in the Pacific Ocean are less pronounced than in nature or in POP simulations forced by observed atmospheric conditions, due to the excessive potential vorticity barriers at around 13°N and 10°S in CCSM3. These deficiencies are likely related to the double ITCZ in the model's climatology and the meridional confinement of atmosphere and ocean anomalies associated with ENSO (Deser et al. 2005). In the Atlantic, the Northern Hemisphere pathway is absent in CCSM3, and the flow originating in the Southern Hemisphere is overly concentrated along the western boundary. The model's deficiencies in representing tropical-extratropical connections in both the Atlantic and Pacific likely degrades its simulation of decadal variability over the globe.

Acknowledgements.

We thank Marlos Goes of the University of São Paulo for performing the trajectory analyses in the Atlantic Ocean and Mark Stevens of NCAR for providing the PDO timeseries from CCSM3. Ilana Wainer's contribution was supported under grant CNPq300223/93-7 from the Brazilian government. Computational facilities used to perform the T42 and T85 CCSM3 control simulations were provided by NCAR, which is supported by the National Science Foundation.

References

- Alexander, M. A., and C. Deser, 1995: A mechanism for the recurrence of wintertime midlatitude SST anomalies. *J. Phys. Oceanogr.*, **25**, 122-137.
- Alexander, M. A., C. Deser, and M. S. Timlin, 1999: The re-emergence of SST anomalies in the North Pacific Ocean. *J. Climate*, **12**, 2419-2431.
- Alexander, M. A., I. Blade, M. Newman, J. R. Lanzante, N.-C. Lau, and J. D. Scott, 2002: The atmospheric bridge: The influence of ENSO teleconnections on air-sea interaction over the global oceans. *J. Climate*, **15**, 2205-2231.
- Alexander, M. A., N.-C. Lau, and J. D. Scott, 2004: Broadening the atmospheric bridge paradigm: ENSO teleconnections to the North Pacific in summer and to the tropical west Pacific- Indian Oceans over the seasonal cycle. *Earth Climate: The Ocean-Atmosphere Interaction*, eds. C. Wang, S.-P. Xie and J. Carton. AGU Monograph. pp. 85-104.
- Andelberg, M. R., 1973: Cluster analysis for applications. *Academic Press*, 359pp.
- Barnston, A.G., and R.E. Livezey, 1987. Classification, seasonality and persistence of low frequency atmospheric circulation patterns. *Mon. Wea. Rev.*, **115**, 1083-1126.
- Barsugli, J. J., and D. S. Battisti, 1998: The basic effects of atmosphere-ocean thermal

coupling on midlatitude variability. *J. Atmos. Sci.*, **55**, 477-493.

Benson, A. J., and A. W. Trites, 2002: Ecological effects of regime shifts in the Bering Sea and eastern North Pacific Ocean, *Fish and Fisheries*, **3**, 95-113.

Blackmon, M. L., J. M. Wallace, N.-C. Lau, and S. L. Mullen, 1977: An observational study of the Northern Hemisphere wintertime circulation. *J. Atmos. Sci.*, **34**, 1040-1053.

Branstator, G., 1983: Horizontal energy propagation in a barotropic atmosphere with meridional and zonal structure. *J. Atmos. Sci.*, **40**, 1689-1708.

Branstator, G., 1985: Analysis of general circulation model sea-surface temperature anomaly simulations using a linear model. Part I: Forced solutions. *J. Atmos. Sci.*, **21**, 2225-2241,

Branstator, G., 1995: Organization of storm track anomalies by recurring low-frequency circulation anomalies. *J. Atmos. Sci.*, **52**, 207-226.

Branstator, G., 2002: Circumglobal teleconnections, the jet stream waveguide, and the North Atlantic Oscillation. *J. Climate*, **15**, 1893-1910.

Briegleb, B. P., C. M. Bitz, E. C. Hunke, W. H. Lipscomb, M. M. Holland, J. L. Schramm, and R. E. Moritz, 2004: Scientific description of the sea ice component in the

Community Climate System Model, Version Three. NCAR Tech. Note NCAR/TN-463+STR, 70 pp.

Cassou, C., and L. Terray, 2001: Oceanic forcing of the wintertime low frequency atmospheric variability in the North Atlantic European sector: a study with the ARPEGE model. *J. Climate*, **14**, 4266-4291.

Cassou, C., C. Deser, L. Terray, J. W. Hurrell, and M. Drévillon, 2004a: Summer sea surface temperature conditions in the North Atlantic and their impact upon the atmospheric circulation in early winter. *J. Climate*, **17**, 3349-3363.

Cassou, C., L. Terray, J. W. Hurrell, and C. Deser, 2004b: North Atlantic winter climate regimes: spatial asymmetry, stationarity with time and oceanic forcing. *J. Climate*, **17**, 1055-1068.

Cayan, D.R., 1992: Latent and sensible heat flux anomalies over the northern oceans: driving the sea surface temperature. *J. Phys. Oceanogr.*, **22**, 859-881.

Chang, E. K. M., S. Lee, and K. L. Swanson, 2002: Storm track dynamics. *J. Climate*, **15**, 2163-2183.

Collins, W. D., M. Blackmon, C. Bitz, G. B. Bonan, C. S. Bretherton, J. A. Carton, P. Chang, S. Doney, J. J. Hack, J. T. Kiehl, T. Henderson, W. G. Large, D. McKenna, B. D. Santer,

and R. Smith, 2005a: The Community Climate System Model: CCSM3. *J. Climate*, this issue.

Collins, W. D., P. J. Rasch, B. A. Boville, J. J. Hack, J. R. McCaa, D. L. Williamson, B. Briegleb, C. M. Bitz, S.-J. Lin, and M. Zhangns, W. D., 2005b: The formulation and atmospheric simulation of the Community Atmosphere Model:CAM3. *J. Climate*, this issue.

de Cöetlogon, G., and C. Frankignoul. 2003: The persistence of winter sea surface temperature in the North Atlantic. *J. Climate*, **16**, 1364-1377.

Danabasoglu, G., W. G. Large, J. J. Tribbia, P. R. Gent, B. P. Briegleb, and J. C. McWilliams, 2005: Diurnal ocean-atmosphere coupling. *J. Climate.*, this issue.

Deser, C., M. Alexander, and M. Timlin, 2003: Understanding the persistence of sea surface temperature anomalies in midlatitudes. *J. Climate.*, **16**, 57-72.

Deser, C., and M. L. Blackmon, 1995: On the relationship between Tropical and North Pacific sea surface temperature variations. *J. Climate*, **8**, 1677-1680.

Deser, C., M. A. Alexander, and M. S. Timlin, 1999: Evidence for a wind-driven intensification of the Kuroshio Current extension from the 1970s to the 1980s. *J. Climate*, **9**, 1840-1855.

Deser, C., A. Capotondi, R. Saravanan, and A. Phillips, 2005: Tropical Pacific and Atlantic Climate Variability in CCSM3. *J. Climate*, this issue.

Deser, C., A. S. Phillips and J. W. Hurrell, 2004: Pacific interdecadal climate variability: linkages between the tropics and the North Pacific during boreal winter since 1900. *J. Climate*, **17**, 3109-3124.

DeWeaver, E., and S. Nigam, 2002: Linearity in ENSO's atmospheric response. *J. Climate*, **15**, 2446-2461.

Frankignoul, C., P. Muller, and E. Zorita, 1997: A simple model of the decadal response of the ocean to stochastic wind forcing. *J. Phys. Oceanogr.*, **27**, 1533-1546.

Frankignoul, C., and E. Kestenare, 2002: The surface heat flux feedback. Part I: estimates from observations in the Atlantic and the North Pacific. *Climate Dyn.*, **19**, 633-647.

Graham, N. E., T. P. Barnett, R. Wilde, M. Ponater, and S. Schubert, 1994: Low-frequency variability in the winter circulation over the Northern Hemisphere. *J. Climate.*, **7**, 1416-1442.

Gu, D., and S. G. H. Philander, 1997: Interdecadal climate fluctuations that depend on the exchanges between the Tropics and extratropics. *Science*, **240**, 1293-1302.

- Hahn, C. J., and S. G. Warren, 1999: Extended edited synoptic cloud reports from ships and land stations over the globe, 1952- 1996. NDP026C, Carbon Dioxide Information Analysis Center, Oak Ridge National Laboratory, Oak Ridge, TN, 71 pp. [Available online at <http://cdiac.esd.ornl.gov/epubs/ndp/ndp026c/ndp026c.html>.]
- Harnik, N., and E. K. M. Chang, 2003: Storm track variations as seen in radiosonde observations and reanalysis data. *J. Climate*, **16**, 480-495.
- Hazeleger, W., P. de Vries, and Y. Friocourt, 2003: Sources of the equatorial undercurrent in the Atlantic in a high-resolution ocean model, *J. Phys. Oceanogr.*, **33**, 677-693.
- Hoerling, M. P., A. Kumar, and M. Zhong, 1997: El Niño, La Niña and the nonlinearity of their teleconnections. *J. Climate*, **10**, 1769-1786.
- Hoskins, B.J., A.J. Simmons, and D.C. Andrews, 1977: Energy dispersion in a barotropic atmosphere. *Quart. J. Roy. Meteor. Soc.*, **103**, 553-567.
- Hoskins B.J., and T. Ambrizzi, 1993: Rossby wave propagation on a realistic longitudinally varying flow. *J. Atmos. Sci.*, **50**, 1661-1671.
- Hurrell, J. W., J. J. Hack, A. Philips, J. Caron, and J. Yin, 2005: The dynamical simulation of the NCAR Community Atmosphere Model version 3 (CAM3). *J. Climate*, this issue.

Iwasaka, N., and J. M. Wallace, 1995: Large scale air sea interaction in the Northern Hemisphere from a view point of variations of surface heat flux by SVD analysis., *J. Meteor. Soc. Japan*, **73**, 781-794.

Jin, F.-F., 1997: A theory of interdecadal climate variability of the North Pacific ocean-atmosphere system . *J. Climate*, **10**, 1821-1835.

Johnson, G. C., and M. J. McPhaden, 1999: Interior pycnocline flow from the subtropical to the equatorial Pacific Ocean. *J. Phys. Oceanogr.*, **29**, 3073-3089.

Kalnay, E., M. Kanamitsu, R. Kistler, W. Collins, D. Deaven, L. Gandin, M. Iredell, S. Saha, G. White, J. Woollen, Y. Zhu, M. Chelliah, W. Ebisuzaki, W. Higgins, J. Janowiak, K. C. Mo, C. Ropelewski, J. Wang, A. Leetmaa, R. Reynolds, R. Jenne, and D. Joseph, 1996: The NCEP/NCAR 40-year reanalysis project. *Bull. Amer. Meteor. Soc.*, **77**, 437-471.

Kaplan A., Y. Kushnir, and M. A. Cane, 2000: Reduced space optimal interpolation of historical marine sea level pressure: 1854-1992. *J. Climate*, **13**, 2987-3002.

Kleeman, R., J. P. McCreary, and B. A. Klinger, 1999: A mechanism for the decadal variation of ENSO. *Geophys. Res. Lett.*, **26**, 743-747.

Kushnir, Y., W.A. Robinson, I. Blade, N.M.J. Hall, S. Peng, and R. Sutton, 2002: Atmospheric GCM response to extratropical SST anomalies: Synthesis and evaluation. *J. Climate*, **15**, 2233-2256.

Large, W. G. and G. Danabasoglu, 2005: Attribution and impacts of upper ocean biases in CCSM3. *J. Climate*, this issue.

Latif, M., and T. P. Barnett, 1994: Causes of decadal climate variability over the North Pacific and North America. *Science*, **266**, 634-637.

Latif, M., and T. P. Barnett, 1996: Decadal climate variability over the North Pacific and North America: Dynamics and predictability. *J. Climate*, **9**, 2407-2423.

Lau, N.-C., 1981: A diagnostic study of recurrent meteorological anomalies appearing in a 15-year simulation with a GFDL general circulation model. *Mon. Wea. Rev.*, **109**, 2287-2311.

Lau, N.-C., 1988: Variability of the observed midlatitude stormtracks in relation to low-frequency changes in the circulation pattern. *J. Atmos. Sci.*, **45**, 2718-2743.

Levitus, S., T.P. Boyer, M.E. Conkright, T. O' Brien, J. Antonov, C. Stephens, L. Stathoplos, D. Johnson, and R. Gelfeld, 1998: NOAA Atlas NESDIS 18, World Ocean Database 1998: Vol. 1: Introduction, U.S. Gov. Printing Office, Wash., D.C., 346pp.

Lin, H., and J. Derome, 2004: Nonlinearity of the extratropical response to tropical forcing. *J. Climate*, **17**, 2597-2608.

Mantua, N. J., S. R. Hare, Y. Zhang, J. M. Wallace and R. Francis, 1997: A Pacific interdecadal climate oscillation with impacts on salmon production. *Bull. Amer. Meteor. Soc.*, **78**, 1069-1079.

McPhaden, M. J., and D. Zhang, 2002: Slowdown of the meridional overturning circulation in the upper Pacific Ocean. *Nature*, **415**, 603-608.

Michelangeli, P., R. Vautard, and B. Legras, 1995: Weather regime recurrence and quasi-stationarity. *J. Atmos. Sci.*, **52**, 1237-1256.

Miller, A. J., and N. Schneider, 2000: Interdecadal climate regime dynamics in the North Pacific Ocean: Theories, observations and ecosystem impacts. *Progress in Oceanography*, **27**, 257-260.

Miller, A. J., D. R. Cayan, T. P. Barnett, N. E. Graham, and J. M. Oberhuber, 1994: Interdecadal variability of the Pacific Ocean: Model response to observed heat flux and wind stress anomalies. *Climate Dyn.*, **9**, 287-302.

Miller, A. J., D. R. Cayan, and W. B. White, 1998: A westward-intensified decadal change in the North Pacific thermocline and gyre-scale circulation. *J. Climate*, **11**, 3112-3127.

Molinari, R., S. Bauer, D. Snowden, G. Johnson, B. Bourles, Y. Gouriou, and H. Mercier, 2003: A comparison of kinematic evidence for tropical cells in the Atlantic and Pacific

oceans. *Interhemispheric Water Exchange in the Atlantic Ocean*. eds. G. Goni and P. Malanotte-Rizzoli, Elsevier Oceanographic Series, 269-286 pp..

Monterey, G. I., and S. Levitus, 1997: Seasonal Variability of Mixed Layer Depth for the World Ocean. NOAA NESDIS Atlas 14, U.S. Gov. Printing Office, Wash., D.C., 5 pp.

Murray, R. J., and I. Simmonds, 1991: A numerical scheme for tracking cyclone centres from digital data. Part I: Development and operation of the scheme. *Aust. Meteor. Mag.*, **39**, 155-166.

Nakamura, H., G. Lin, and T. Yamagata, 1997: Decadal climate variability in the North Pacific during the recent decades. *Bull. Amer. Met. Soc.*, **78**, 2215-2225.

Namias, J., and R. M. Born, 1970: Temporal coherence in North Pacific sea-surface temperature patterns. *J. Geophys. Res.*, **75**, 5952-5955.

Namias, J. and R. M. Born, 1974: Further studies of temporal coherence in North Pacific sea surface temperatures. *J. Geophys. Res.*, **79**, 797-798.

Neiman, P. J., and M. A. Shapiro. 1993: The life cycle of an extratropical marine cyclone. Part I: Frontal-cyclone evolution and thermodynamic air-sea interaction. *Mon. Wea. Rev.*, **121**, 2153-2176.

- Newman, M., G. P. Compo, and M. A. Alexander, 2003: ENSO-forced variability of the Pacific Decadal Oscillation. *J. Climate*, **16**, 3853-3857.
- Norris, J. R., and C. B. Leovy, 1994: Interannual variability in stratiform cloudiness and sea surface temperature. *J. Climate*, **7**, 1915-1925.
- Norris, J. R., 1998: Low cloud type over the ocean from surface observations. Part II: geographical and seasonal variations. *J. Climate*, **11**, 383-403.
- Norris, J. R., Y. Zhang, and J. M. Wallace, 1998: Role of low clouds in summertime atmosphere–ocean interactions over the North Pacific. *J. Climate*, **11**, 2482-2490.
- Norris, J. R., 2000: Interannual and interdecadal variability in the storm track, cloudiness, and sea surface temperature over the summertime North Pacific. *J. Climate*, **13**, 422-430.
- Norris, J. R., and S. A. Klein, 2000: Low cloud type over the ocean from surface observations. Part III: relationship to vertical motion and the regional surface synoptic environment. *J. Climate*, **13**, 245-256.
- Norris, J. R., and C. P. Weaver, 2001: Improved techniques for evaluating GCM cloudiness applied to the NCAR CCM3. *J. Climate*, **14**, 2540-2550.

Norris, J. R., and S. F. Iacobellis, 2004: Summertime North Pacific cloud feedbacks inferred from synoptic-scale dynamic and thermodynamic relationships. *J. Climate*, submitted.

Oleson, K. W., Y. Dai, G. Bonan, M. Bosilovich, R. Dickinson, P. Dirmeyer, F. Hoffman, P. Houser, S. Levis, G.-Y. Niu, P. Thornton, M. Vertenstein, Z.-L. Yang, and X. Zeng, 2004: Technical description of the Community Land Model (CLM). NCAR Tech. Note NCAR/TN-461+STR, 174 pp.

Park, S., C. Deser, and M. A. Alexander, 2004: Estimation of surface heat flux feedback over the global ocean using ship-observed turbulent heat flux and satellite-derived radiative flux data. *J. Climate*, submitted.

Powell, M. J. D., 1964: An efficient method for finding the minimum of a function of several variables without calculating derivatives. *Comp. J.*, **7**, 155-162.

Rayner, N. A., D. E. Parker, E. B. Horton, C. K. Folland, L. V. Alexander, D. P. Rowell, E. C. Kent, and A. Kaplan, 2003: Global analyses of sea surface temperature, sea ice, and night marine air temperature since the late nineteenth century. *J. Geophys. Res.*, **108**, 4407, doi:10.1029/2002JD002670

Robertson, A.W. and M. Ghil, 1999: Large-scale weather regimes and local climate over the western United States. *J. Climate*, **12**, 1796-1813.

Roden, G. I., 1998: Upper ocean thermohaline, oxygen, nutrient and flow structure near the date line of the summer of 1993. *J. Geophys. Res.*, **105(C6)**, 12,919-12,939.

Schneider, N., and B. D. Cornuelle, 2005: The forcing of the Pacific Decadal Oscillation, *J. Climate*, submitted.

Schneider, N., and A. J. Miller, 2001: Predicting western North Pacific Ocean climate. *J. Climate.*, **14**, 3997-4002.

Schneider, N., A. J. Miller, and D. W. Pierce, 2002: Anatomy of North Pacific decadal variability. *J. Climate*, **15**, 586-605.

Stephenson, D.B., A. Hannachi, and A. O'Neill, 2004: On the existence of multiple climate regimes. *Quart. J. Roy. Met. Soc.*, **130**, 583-605.

Stevens, M., W. Collins, J. Hack, P. Rasch, cited 2005: CCSM3 coupled model development runs. [Available online at <http://www.cgd.ucar.edu/cms/stevens/ccsm3/ccsm3.T85.html>.]

Straus, D. M., and J. Shukla, 2002: Does ENSO Force the PNA? *J. Climate*, **15**, 2340-2358.

Sturges, W., and B. G. Hong, 1995: Wind forcing of the Atlantic thermocline along 32°N at low frequencies. *J. Phys. Oceanogr.*, **25**, 1706-1715.

- Terray, L., M. E. Demory, M. Dequé, G. deCoetlogon., and E. Maisonnavé, 2004: Simulation of Late-Twenty-First-Century changes in wintertime atmospheric circulation over Europe due to anthropogenic causes. *J. Climate*, in press.
- Thompson, D. W. J., and J. M. Wallace, 1998: The Arctic Oscillation signature in the wintertime geopotential height and temperature fields. *Geophys. Res. Lett.*, **25**, 1297-1300.
- Timlin, M., M. A. Alexander, and C. Deser, 2002: On the reemergence of North Atlantic SST anomalies. *J. Climate.*, **15**, 2707-2712.
- Trenberth, K. E., 1990: Recent observed interdecadal climate changes in the Northern Hemisphere. *Bull. Amer. Meteor. Soc.*, **71**, 988-993.
- Trenberth, K. E., and J. W. Hurrell, 1994: Decadal atmosphere-ocean variations in the Pacific. *Climate Dyn.*, **9**, 303-319.
- Tselioudis, G., and C. Jakob, 2002: Evaluation of midlatitude cloud properties in a weather and a climate model: dependence on dynamic regime and spatial resolution. *J. Geophys. Res.*, **107**, 4781, doi:10.1029/2002JD002259.
- Wallace, J.M. and D. Gutzler, 1981: Teleconnections in geopotential fields during the Northern Hemisphere winter. *Mon. Wea. Rev.*, **109**, 784-812.

- Watanabe, M., and M. Kimoto, 2000: On the persistence of decadal SST anomalies in the North Atlantic. *J. Climate.*, **13**, 3017-3028.
- Weare, B. C., 1994: Interrelationships between cloud properties and sea surface temperatures on seasonal and interannual time scales. *J. Climate*, **7**, 248-260.
- Wyant, M. C., C. S. Bretherton, H. A. Rand, and D. E. Stevens, 1997: Numerical simulations and a conceptual model of the stratocumulus to trade cumulus transition. *J. Atmos. Sci.*, **54**, 168-192.
- Yin, J. H., and D. S. Battisti, 2004: Why do baroclinic waves tilt poleward with height? *J. Atmos. Sci.*, **61**, 1454-1460.
- Zhang, D., M. J. McPhaden, and W. E. Johns and, 2003: Observational evidence for flow between the subtropical and tropical Atlantic: the atlantic subtropical cells. *J. Phys. Oceanogr.*, **33**, 1783-1797.
- Zorita E. and C. Frankignoul. 1997: Modes of North Atlantic decadal variability in the ECHAM1/LSG Coupled ocean-atmosphere general circulation model. *J. Climate*, **10**, 183-200.

Table 1: Relative change (%) of occurrence of the four regimes for El Niño/La Niña events and for the positive and negative phase of the PDO. El Niño (La Niña) years are quantified from the Niño 3.4 SST index, selecting events exceeding (below) the 90th (10th) percentile. Decadal PDO periods are estimated from the time series of the leading EOF of DJFM SST performed over the Pacific north of 20°N. Bold stands for significant values (at the 95% level) based on random reshuffling of the total sample.

	PNA+	PNA-	ALE+	ALE-
El Niño	+18	-38	-22	+40
La Niña	-50	+64	+18	-24
PDO+	+16	-11	-19	+16
PDO-	-11	+19	+1	-8

Figure Captions:

Fig. 1. Cyclone trajectory counts during DJFM for (a) ERA-40 for years 1958-2000, (b) CCSM3 for years 501-540. The contour interval is every 3 cyclones per year within a 500 km distance of a given point.

Fig. 2. ENSO's impact on the storm tracks as given by the composite difference trajectory counts in DJFM for the ten strongest El Niño events minus the ten strongest La Niña events for (a) ERA-40 during years 1958-2000, (b) CCSM3 during years 501-540. The El Niño (La Niña) events are determined from the years with the warmest (coldest) SSTs in the Niño3.4 region (5°N-5°S, 170°W-120°W). The contour interval is every 1 cyclone per year within a 500 km distance of a given point. Hatching indicates differences that are significant at the 95% level as indicated by the t statistic.

Fig. 3. DJFM 2-8 day filtered 300 hPa z'^2 (thick contours) from years 100-600 of the CCSM3 T85 control run, regressed on the following PCs of DJFM 2-8 day 300 hPa z'^2 : (a) North Pacific PC1 (25.1% variance explained), (b) North Pacific PC2 (17.4%), (c) North Atlantic PC1(26.3%), (d) North Atlantic PC2 (16.7%). The North Pacific domain is (120°E-120°W, 20°N-80°N) and the North Atlantic domain is (90°W-30°E, 20°N-80°N). The contour interval is 250 m². Stippled contours show the climatological 300 hPa z'^2 , with a contour interval of 2000 m², starting at 6000 m².

Fig. 4. As in Fig. 3, but for DJFM 2-8 day 300 hPa z'^2 for years 1958-2000 of ERA-40,

regressed on the following PCs of DJFM 2-8 day 300 hPa z'^2 : (a) North Pacific PC2 (21.7% variance explained), (b) North Pacific PC1(27.4%), (c) North Atlantic PC 2 (20.5%), (d) North Atlantic PC1 (23.4%).

Fig. 5. DJFM surface temperature, (color) and 1000 hPa zonal wind (black contours) from years 101-600 of the CCSM3 T85 control run, regressed on the following PCs of DJFM 2-8 day 300 hPa z'^2 : (a) North Pacific PC1, (b) North Pacific PC2, (c) North Atlantic PC1, (d) North Atlantic PC2. The contour interval for surface temperature is 0.1°C , and the contour interval for 1000 hPa zonal wind is 0.5 m s^{-1} , with the zero contour omitted. Surface temperature is the equivalent to SST at ice free ocean grid points.

Fig. 6. DJFM surface temperature (color) and ERA-40 1000 hPa zonal wind (black contours) for years 1958-2000 from ERA-40, regressed on the following PCs of DJFM 2-8 day 300 hPa z'^2 from ERA-40: (a) North Pacific PC2, (b) North Pacific PC1 (c) North Atlantic PC2, (d) North Atlantic PC1. The contour interval for surface temperature is 0.1°C , and the contour interval for 1000 hPa zonal wind is 0.5 m s^{-1} , with the zero contour omitted.

Fig. 7. JJA surface temperature (color) and 2-8 day 300 hPa z'^2 (black contours) from years 101-600 of the CCSM3 T85 control run, regressed on the following PCs of JJA 2-8 day 300 hPa z'^2 : (a) North Pacific PC1 (23.1% variance explained) and (c) North Atlantic PC1 (25.1%); JJA surface temperature (color) and 2-8 day 300 hPa z'^2 (black contours) during years 1958-2000 from ERA-40, regressed on the following PCs of JJA 2-8 day 300 hPa z'^2

(b) North Pacific PC1 (17.2%) and (d) North Atlantic PC1 (21.7%). The contour interval for surface temperature is 0.1°C , and the contour interval for 300 hPa z^2 is 250 m^2 , with the zero contour omitted.

Fig. 8. Linear correlation between JJA seasonal anomalies in low-level cloud cover and SST from observations (top) and the coupled control run of CCSM3 (bottom). Observed correlations are for 1958-97 and CCSM3 correlations are the median of twelve 40-year realizations (years 100-579). Open circles mark where all realizations have correlations more negative than the observations and solid circles mark where all realizations have correlations more positive. Contour interval is 0.1, solid lines indicate negative values, dashed lines positive values, and the zero line is thicker. Values between -0.3 and -0.5 are shaded light gray and values below -0.5 are shaded dark gray.

Fig. 9. As in Fig. 8, but for the correlation between low-level cloud cover and near-surface meridional wind component. Values above 0.3 are cross-hatched.

Fig. 10. Correlations between interannual variations in CCSM3 monthly mean January 300 hPa streamfunction with variations in the same quantity at 33°N , 127.5°E . In this diagram as well as in Figs. 11 and 12, the effect of tropical SST anomalies has been filtered from the fields using a regression method described in the text. Also, for these same diagrams, fields have been smoothed by truncating spectrally to R15, transforming to a 48×40 Gaussian grid, and then averaging nine neighboring points. Contour interval is 0.1.

Fig. 11. Correlations between interannual variations in CCSM3 monthly mean January 300

hPa streamfunction at 33°N , 127.5°E and monthly mean January variations in a) sea level pressure, b) surface temperature (which equals SST at ocean points), c) surface latent heat flux into the atmosphere, and d) surface sensible heat flux into the atmosphere. Contour interval is 0.1.

Fig. 12. Correlations between interannual variations in CCSM3 monthly mean January 300 hPa streamfunction at 33°N , 127.5°E and monthly mean surface temperature in a) February and b) March. Contour interval is 0.1.

Fig. 13. (a-d) SLP regimes over the North Pacific in CCSM3 during DJFM. The percentage at the top right of each panel gives the global population of a given cluster over the years 100-599. Contour interval is 2 hPa. (e-h) Simultaneous DJFM surface temperature composites ($^{\circ}\text{C}$) related to the four climate regimes. The events selected for the composite construction correspond to the winters when the regime is dominant. Only significant points based on a two-sided t-test at the 95% level are shown. Contour interval is 0.2°C .

Fig. 14: The a) observed and b) simulated PDO time series in winter, based on the leading principal component of monthly SST anomalies north of 20°N in the Pacific, averaged over November-March. The correlation between the wintertime PDO values and the concurrent near-surface air temperature in c) NCEP reanalysis (1948-2003) and d) the CCSM3 (500-559).

Fig. 15. Same as Fig. 13 but for the regimes in the North Atlantic sector.

Fig 16. The observed and simulated long term mean seasonal cycle of temperature ($^{\circ}\text{C}$, scale at bottom) and MLD (m) in observations (top) and CCSM3 (bottom) in regions of the central North Pacific (35°N - 45°N , 165°E - 175°W) and North Atlantic (50°N - 60°N , 20°W - 40°W). The observed temperature and MLD values are from the World Ocean Atlas (Levitus et al. 1998) and Monterey and Levitus (1997), respectively and the model results from years 350-599 of CCSM3. The observed and model MLD are both based on density criteria, the former the depth at which the density is 0.125 kg m^{-3} greater than at the surface and the latter is the depth of the maximum gradient that is nearest to the surface. Note that the depth scale is different in the Pacific and Atlantic plots.

Fig. 17: The reemergence process in the CCSM3 as indicated by lead-lag regressions ($^{\circ}\text{C}$ per 1°C) between temperature anomalies at the base point, defined here as the 3 top ocean model layers (0-30 m) in FMA and temperature anomalies from the previous January through the following April in the (a) Pacific and (b) Atlantic regions. The contour interval is 0.1 and values >0.5 (<0.4) in (a), and >0.8 (<0.6) in (b) are shaded light (dark).

Fig. 18: Basin-wide reemergence in the CCSM3 across the North Pacific (left) and North Atlantic (right) Oceans as indicated by monthly lead-lag correlations between temperature anomalies located between 65-85 m in August-September, and SST anomalies from the previous January through the following April averaged over 42°N - 52°N . The contour interval is 0.1, and values greater than 0.55 are shaded.

Fig. 19. The (a) first and (b) second EOF of the annual mean depth of the $26.8 \sigma_\theta$ isopycnal for years 350-599 of the CCSM3 T85 control experiment. Values are relative to a one standard deviation change in the corresponding PC. Contour interval is 5 m in (a) and (b). (c) Power spectrum of PC 1 and 2. Also shown are the best fit AR1 spectra and associated 95% and 99% confidence limits.

Fig. 20. The (a) first (b) second EOF of the December-March mean SST for years 350-599 from CCSM3 T85 control experiment. Values are relative to a one standard deviation change in the corresponding PC. The contour interval is 0.2°C .

Fig. 21. Indices averaged over the Kuroshio-Oyashio extension region (35°N - 45°N , 140°E - 180°E). (a) Annual mean depth of the $26.8 \sigma_\theta$ isopycnal. (b) Annual mean SST. (c) Annual mean net surface heat flux. Positive value means heat flux anomaly from ocean to the atmosphere. (d) Annual mean wind stress curl. Positive value means counter-clockwise anomalous wind stress curl.

Fig. 22. (a) Absolute value of potential vorticity (in $10^{-10} \text{ m}^{-1}\text{s}^{-1}$) on the $25 \sigma_\theta$ potential density surface from POP, the ocean component of the CCSM3, forced with observed surface fields over the period 1958-2000. The flow field in the thermocline, shown by the red vectors, is computed by integrating the horizontal velocity components vertically between the 25.5 and $24.5 \sigma_\theta$ potential density surfaces. (b) Same as (a), but from the T85 CCSM3 (years 350-400). Potential vorticity is defined as $(f/(\rho_0))\frac{\partial\rho}{\partial z}$, where f is the

Coriolis parameter, $\frac{\partial \rho}{\partial z}$ is the vertical density gradient, and ρ_0 is a reference density (10^3 kg m^{-1}).

Fig. 23 Lagrangian trajectories along the $25.4 \sigma_\theta$ surface in the a) POP and b) CCSM3 simulations. The trajectories are based on annual averages, the triangles represent the yearly position of floats originally released at the outcrop line in the subtropics, while the vectors indicate the direction of the flow. The trajectories are based on the projection of the velocity field onto an isopycnal surface and, therefore, do not include diapycnal flow.

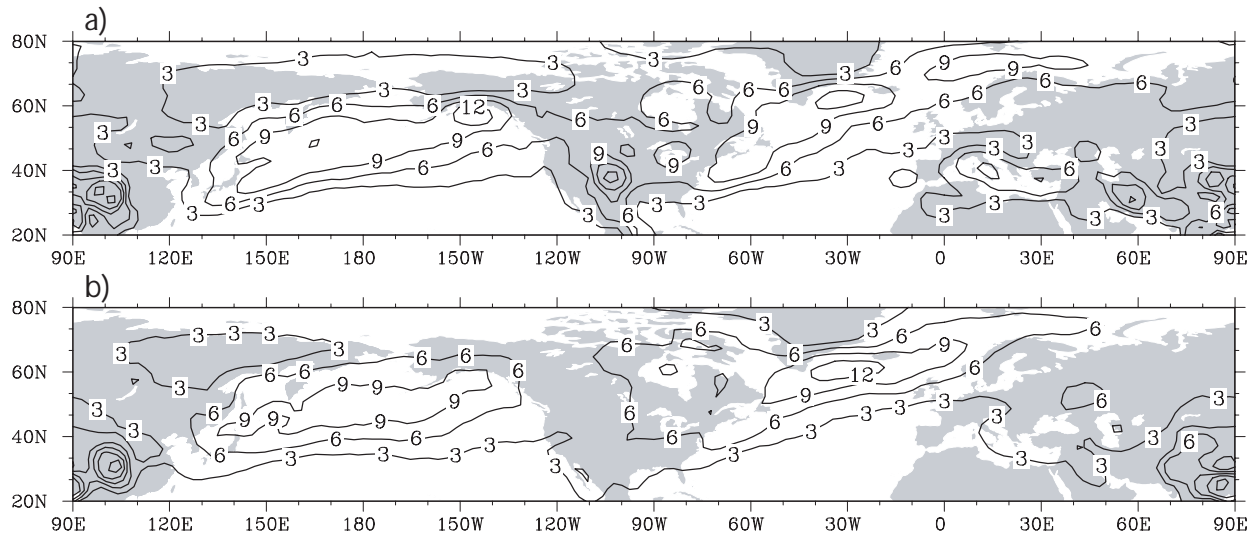


Fig. 1. Cyclone trajectory counts during DJFM for (a) ERA-40 for years 1958-2000, (b) CCSM3 for years 501-540. The contour interval is every 3 cyclones per year within a 500 km distance of a given point.

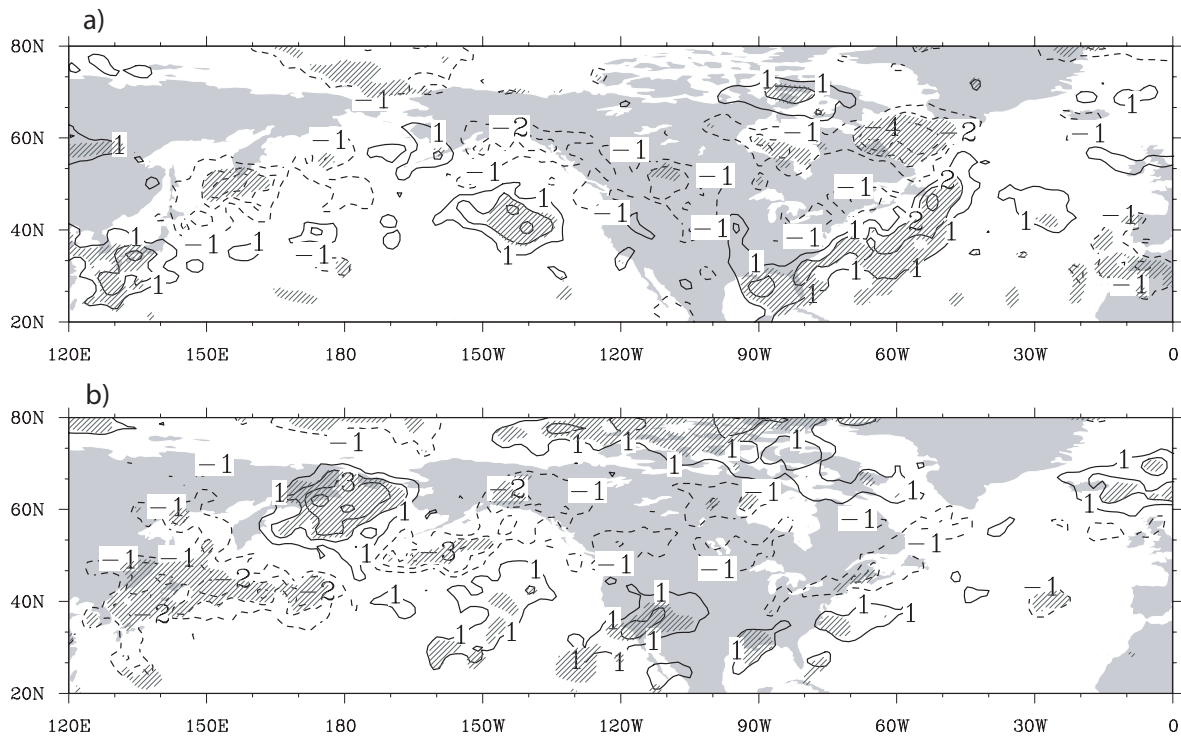


Fig. 2. ENSO's impact on the storm tracks as given by the composite difference trajectory counts in DJFM for the ten strongest El Niño events minus the ten strongest La Niña events for (a) ERA-40 during years 1958-2000, (b) CCSM3 during years 501-540. The El Niño (La Niña) events are determined from the years with the warmest (coldest) SSTs in the Niño3.4 region (5°N-5°S, 170°W-120°W). The contour interval is every 1 cyclone per year within a 500 km distance of a given point. Hatching indicates differences that are significant at the 95% level as indicated by the t statistic.

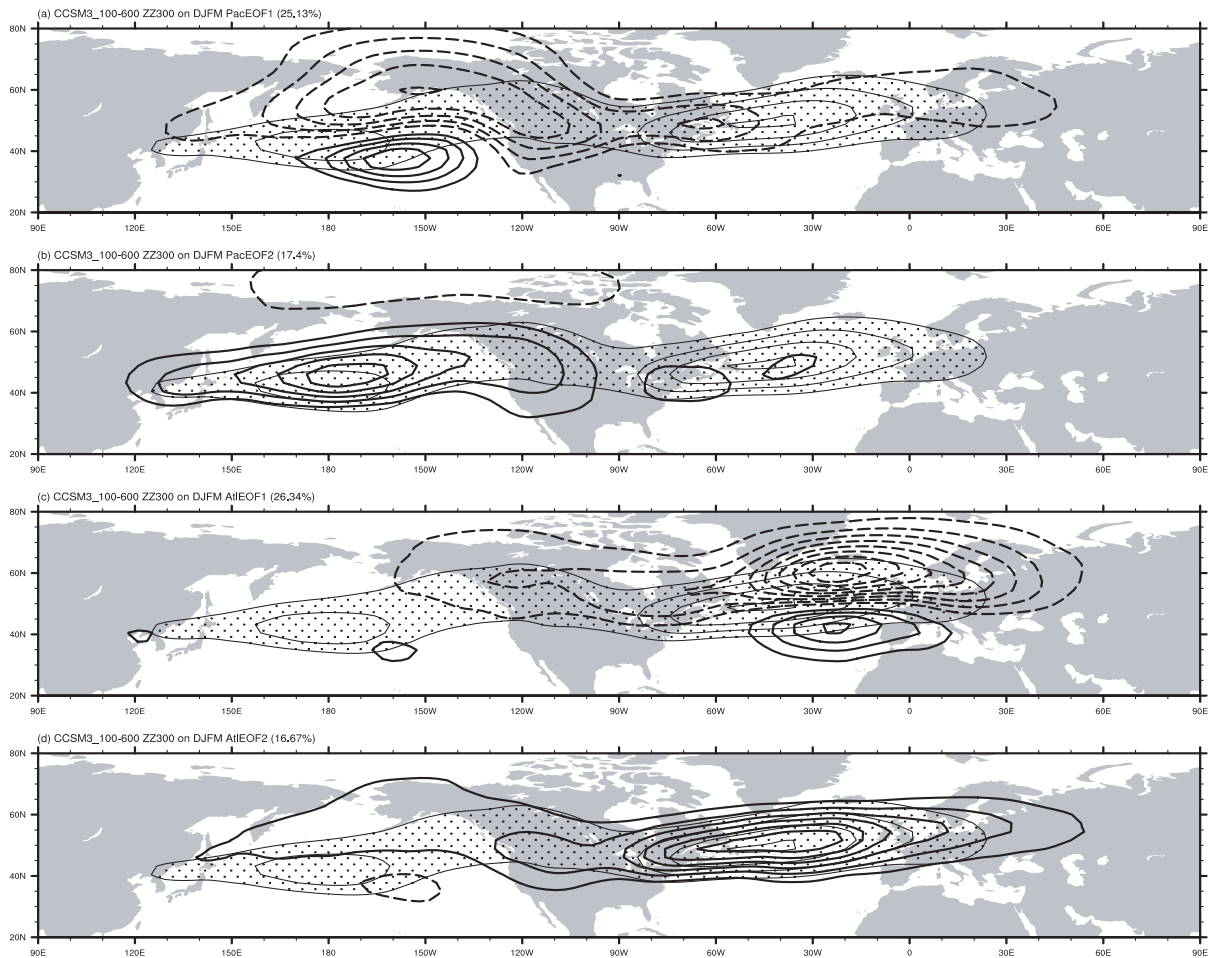


Fig. 3. DJFM 2-8 day filtered 300 hPa z^2 (thick contours) from years 101-600 of the CCSM3 T85 control run, regressed on the following PCs of DJFM 2-8 day 300 hPa z^2 : (a) North Pacific PC1 (25.1% variance explained), (b) North Pacific PC2 (17.4%), (c) North Atlantic PC1(26.3%), (d) North Atlantic PC2 (16.7%). The North Pacific domain is (120°E-120°W, 20°N-80°N) and the North Atlantic domain is (90°W-30°E, 20°N-80°N). The contour interval is 250 m^2 . Stippled contours show the climatological 300 hPa z^2 , with a contour interval of 2000 m^2 , starting at 6000 m^2 .

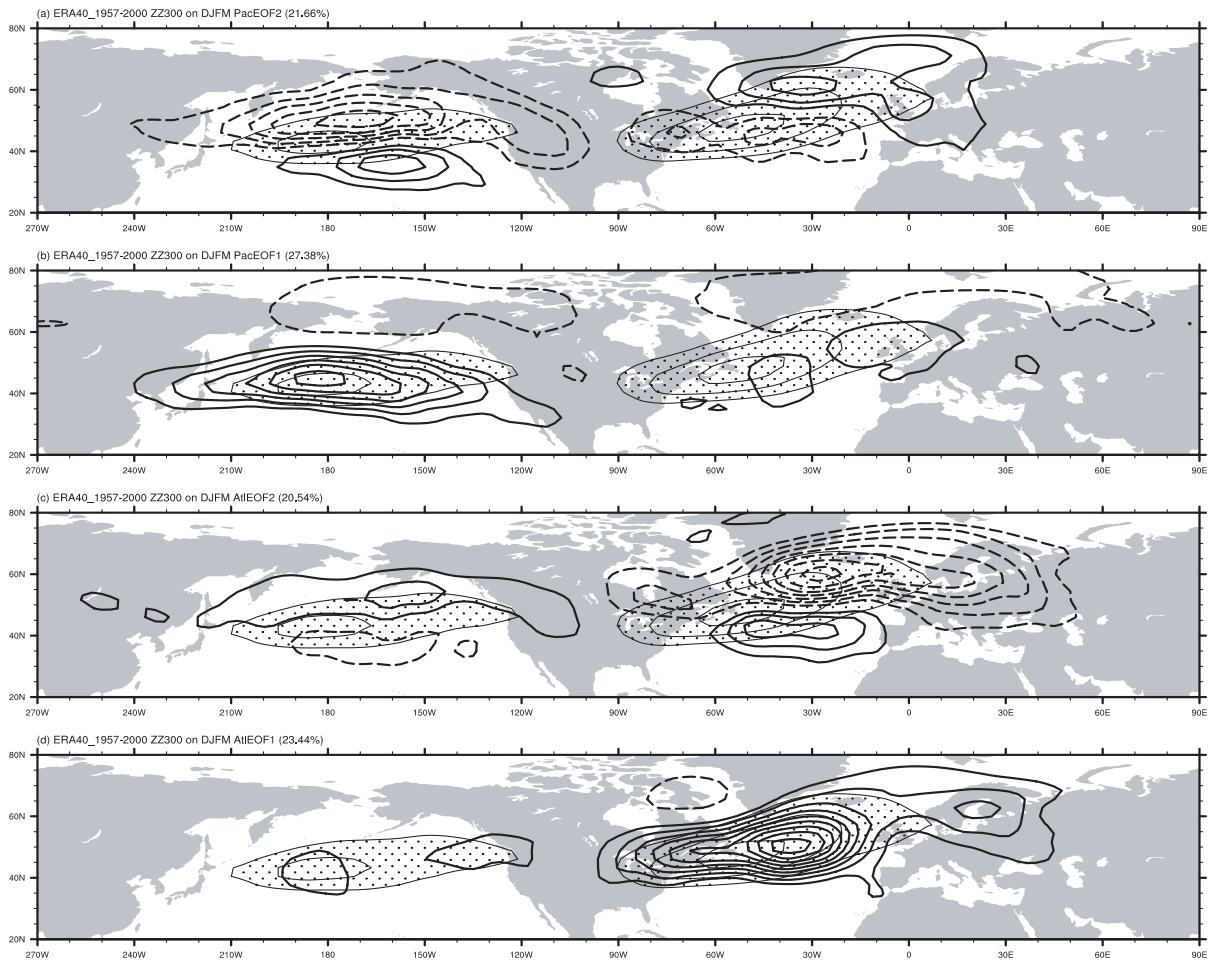


Fig. 4. As in Fig. 3, but for DJFM 2-8 day 300 hPa z^2 from years 1958-2000 of ERA-40, regressed on the following PCs of DJFM 2-8 day 300 hPa z^2 : (a) North Pacific PC2 (21.7% variance explained), (b) North Pacific PC1(27.4%), (c) North Atlantic PC 2 (20.5%), (d) North Atlantic PC1 (23.4%).

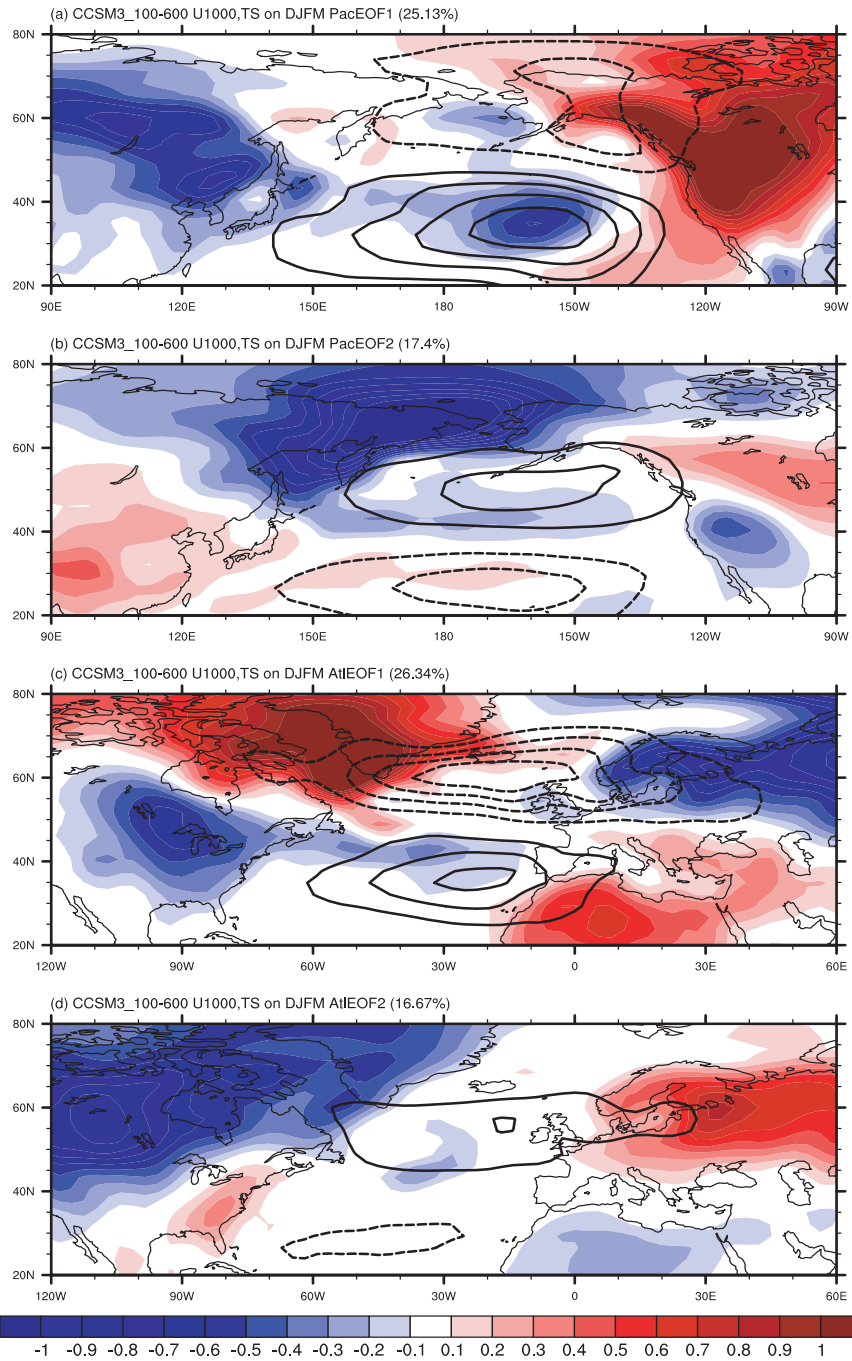


Fig. 5. DJFM surface temperature, (color) and 1000 hPa zonal wind (black contours) from years 101-600 of the CCSM3 T85 control run, regressed on the following PCs of DJFM 2-8 day 300 hPa z^2 : (a) North Pacific PC1, (b) North Pacific PC2, (c) North Atlantic PC1, (d) North Atlantic PC2. The contour interval for surface temperature is 0.1°C , and the contour interval for 1000 hPa zonal wind is 0.5 m s^{-1} , with the zero contour omitted. Surface temperature is the equivalent to SST at ice free ocean grid points.

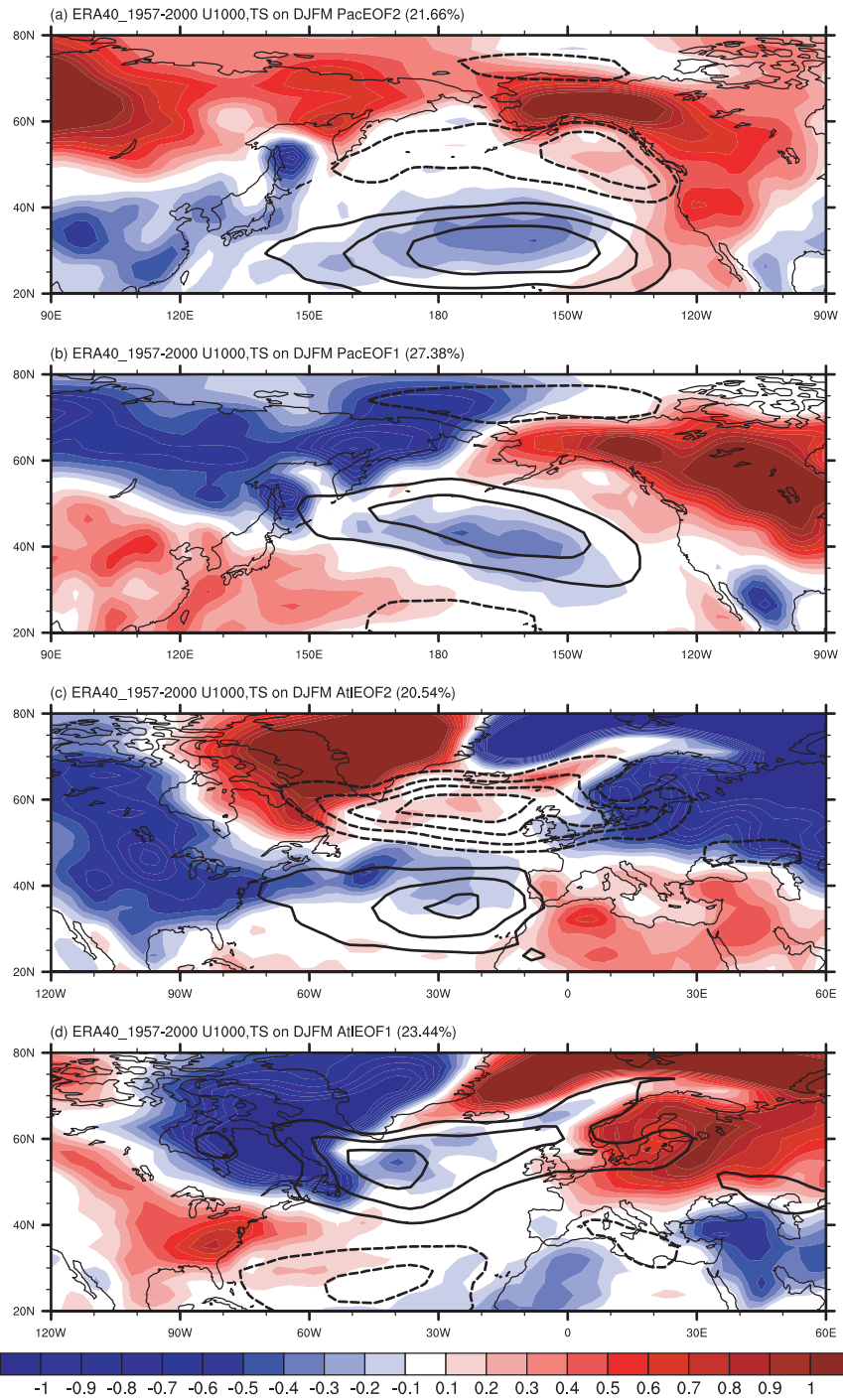


Fig. 6. DJFM surface temperature (color) and ERA-40 1000 hPa zonal wind (black contours) for years 1958-2000 from ERA-40, regressed on the following PCs of DJFM 2-8 day 300 hPa z^2 from ERA-40: (a) North Pacific PC2, (b) North Pacific PC1 (c) North Atlantic PC2, (d) North Atlantic PC1. The contour interval for surface temperature is 0.1°C , and the contour interval for 1000 hPa zonal wind is 0.5 m s^{-1} , with the zero contour omitted.

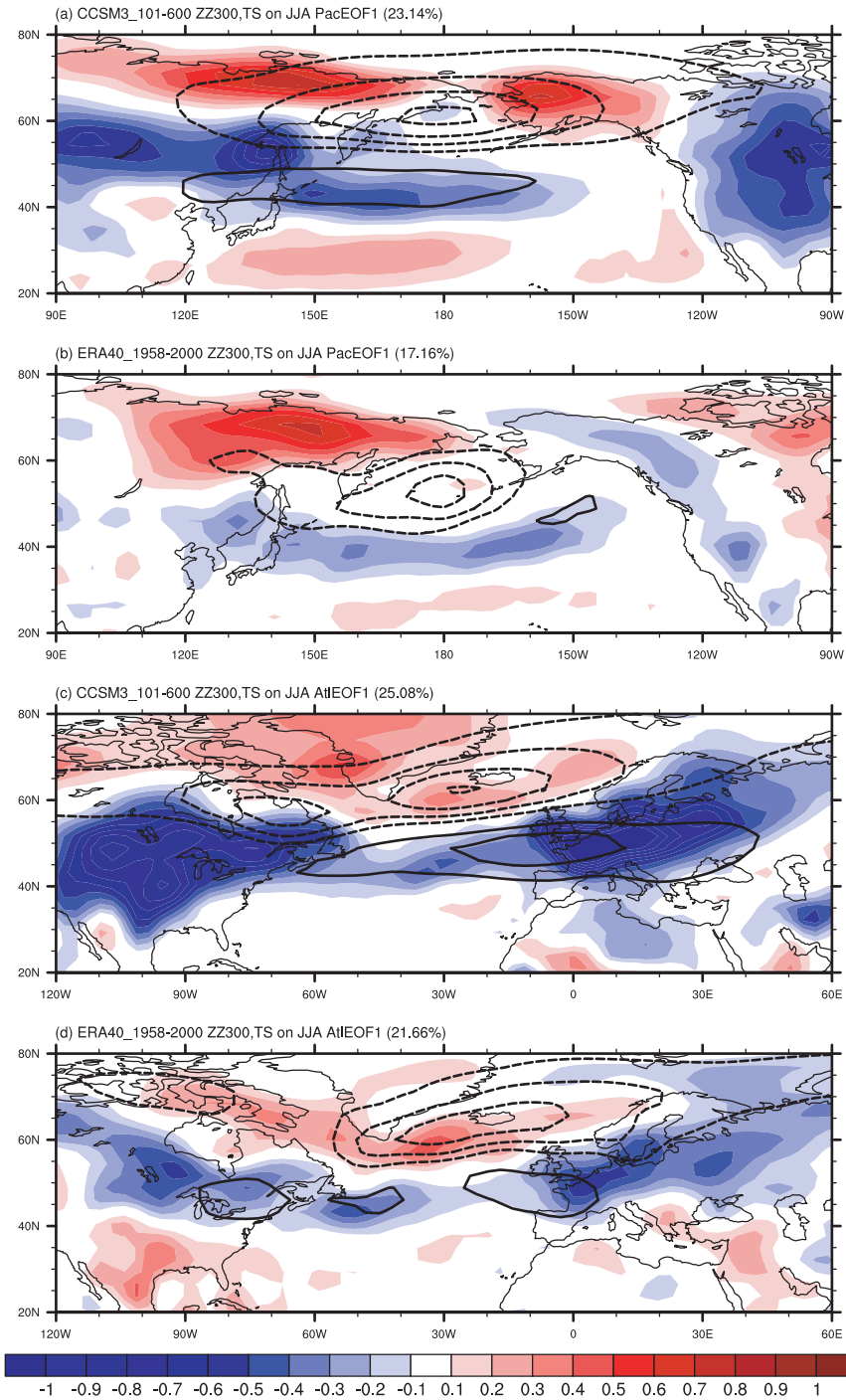


Fig. 7. JJA surface temperature (color) and 2-8 day 300 hPa z^2 (black contours) from years 101-600 of the CCSM3 T85 control run, regressed on the following PCs of JJA 2-8 day 300 hPa z^2 : (a) North Pacific PC1 (23.1% variance explained) and (c) North Atlantic PC1 (25.1%); JJA surface temperature (color) and 2-8 day 300 hPa z^2 (black contours) during years 1958-2000 from ERA-40, regressed on the following PCs of JJA 2-8 day 300 hPa z^2 (b) North Pacific PC1 (17.2%) and (d) North Atlantic PC1 (21.7%). The contour interval for surface temperature is 0.1°C, and the contour interval for 300 hPa z^2 is 250 m², with the zero contour omitted.

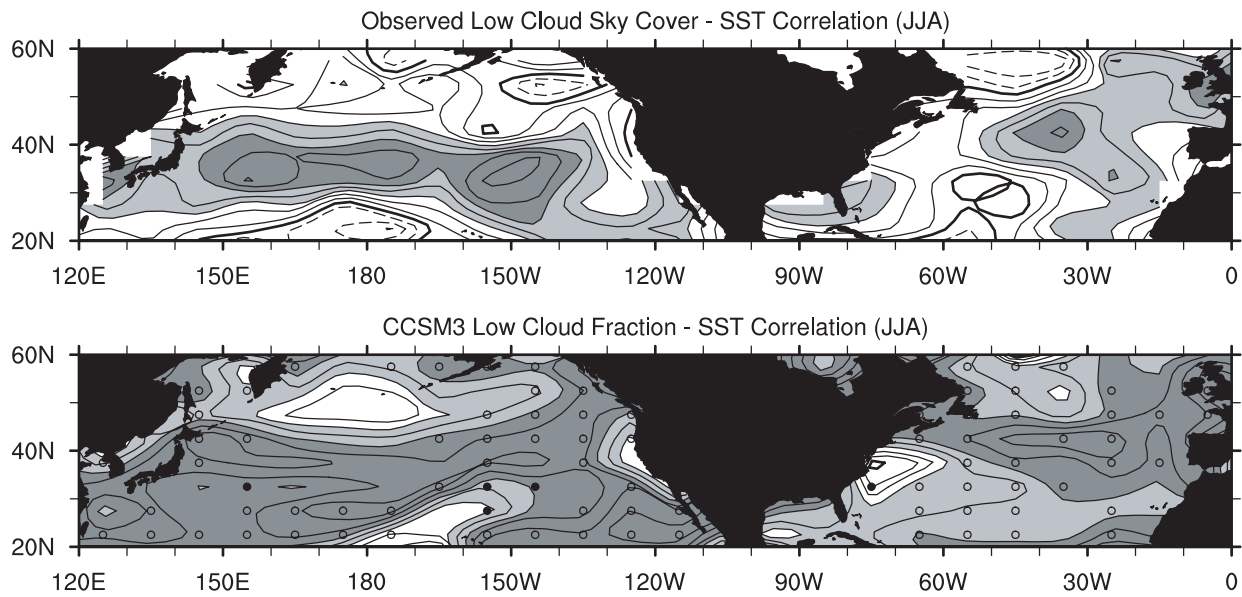


Fig. 8. Linear correlation between JJA seasonal anomalies in low-level cloud cover and SST from observations (top) and the coupled control run of CCSM3 (bottom). Observed correlations are for 1958-97 and CCSM3 correlations are the median of twelve 40-year realizations (years 100-579). Open circles mark where all realizations have correlations more negative than the observations and solid circles mark where all realizations have correlations more positive. Contour interval is 0.1, solid lines indicate negative values, dashed lines positive values, and the zero line is thicker. Values between -0.3 and -0.5 are shaded light gray and values below -0.5 are shaded dark gray.

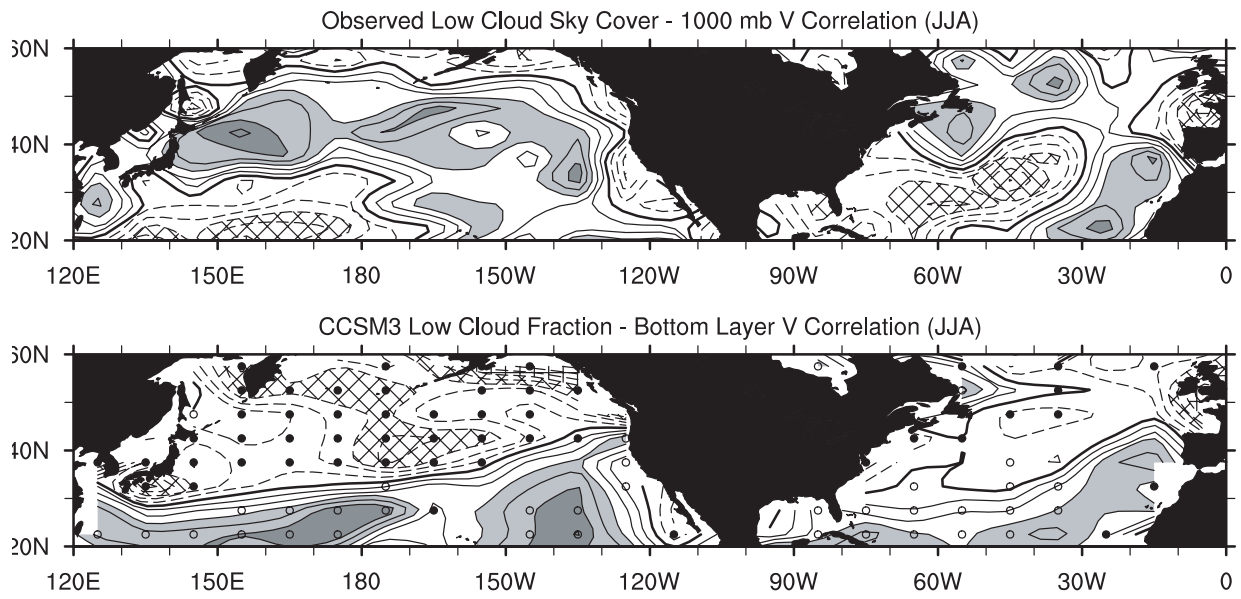


Fig. 9. As in Fig. 8, but for the correlation between low-level cloud cover and near-surface meridional wind component. Values above 0.3 are cross-hatched.

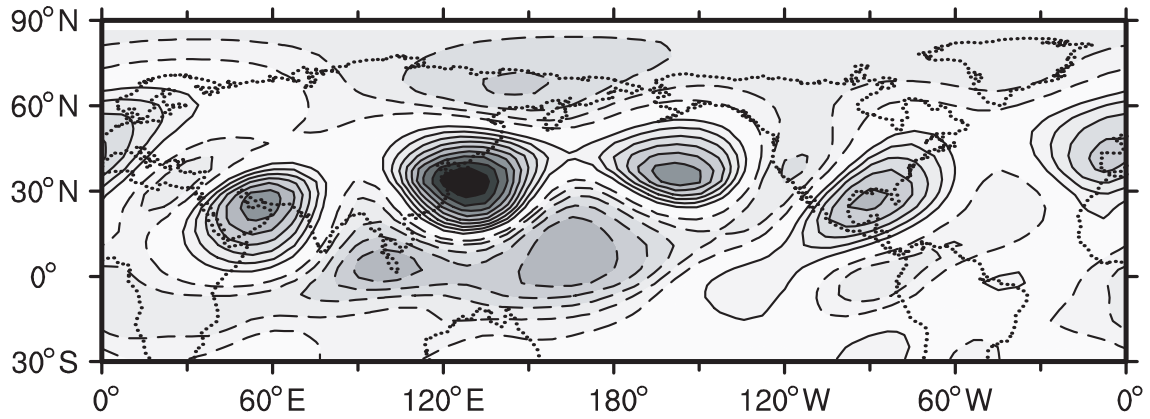


Fig. 10. Correlations between interannual variations in CCSM3 monthly mean January 300 hPa streamfunction with variations in the same quantity at 33°N, 127.5°E. In this diagram as well as in Figs. 11 and 12, the effect of tropical SST anomalies has been filtered from the fields using a regression method described in the text. Also, for these same diagrams, fields have been smoothed by truncating spectrally to R15, transforming to a 48x40 Gaussian grid, and then averaging nine neighboring points. Contour interval is 0.1.

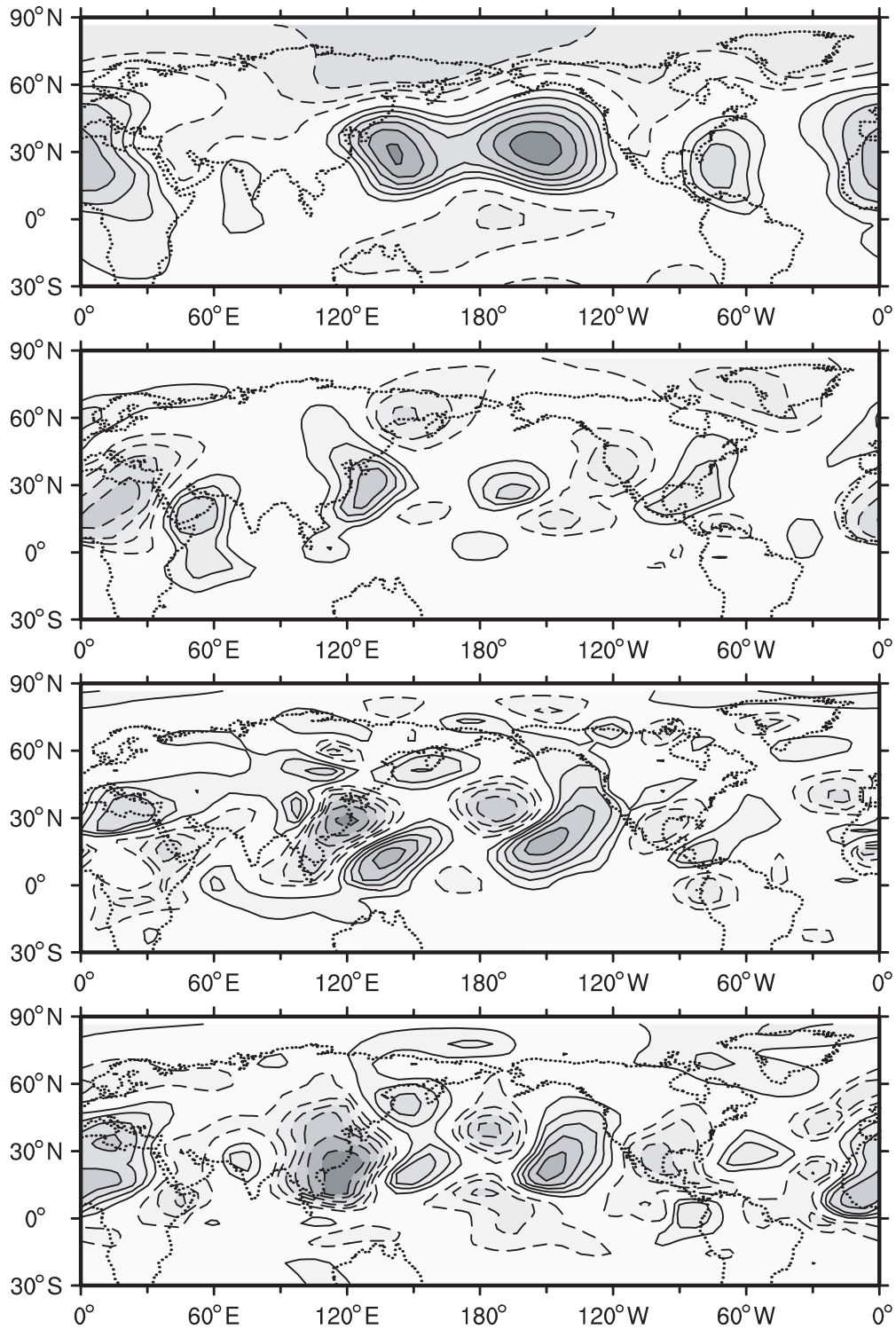


Fig. 11. Correlations between interannual variations in CCSM3 monthly mean January 300 hPa streamfunction at 33°N, 127.5°E and monthly mean January variations in a) sea level pressure, b) surface temperature (which equals SST at ocean points), c) surface latent heat flux into the atmosphere, and d) surface sensible heat flux into the atmosphere. Contour interval is 0.1.

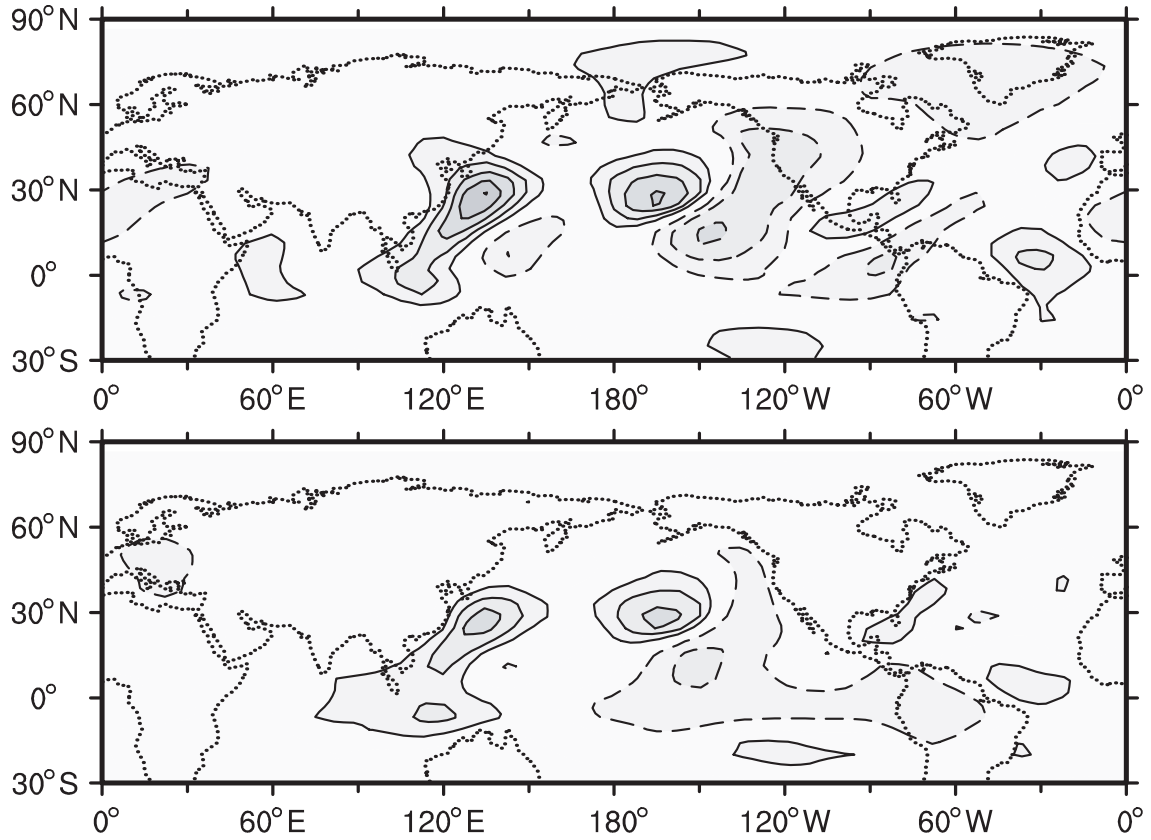


Fig. 12. Correlations between interannual variations in CCSM3 monthly mean January 300 hPa streamfunction at 33°N, 127.5°E and monthly mean surface temperature in a) February and b) March. Contour interval is 0.1.

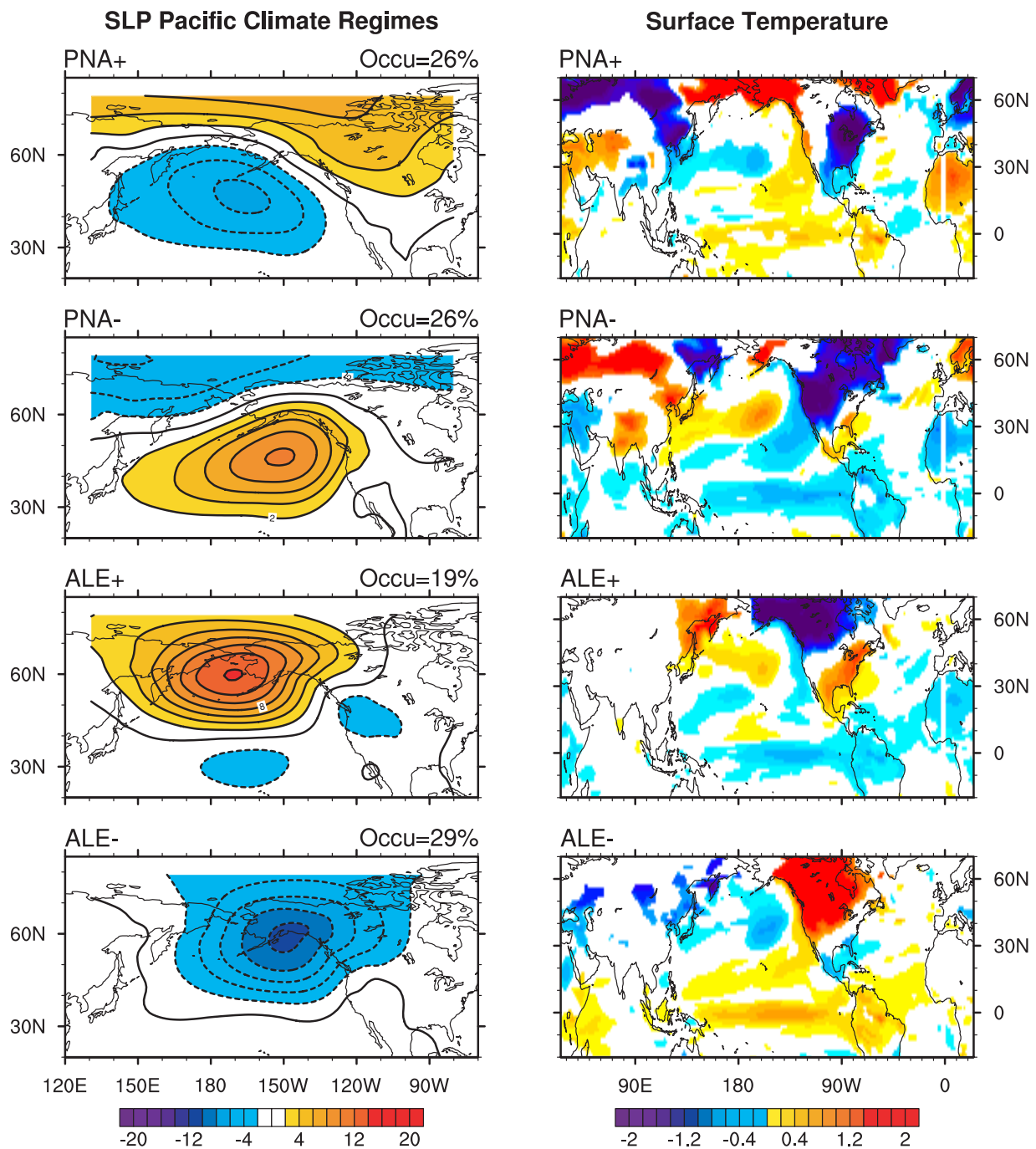


Fig. 13. (a-d) SLP regimes over the North Pacific in CCSM3 during DJFM. The percentage at the top right of each panel gives the global population of a given cluster for years 100-599. Contour interval is 2 hPa. (e-h) Simultaneous DJFM surface temperature composites ($^{\circ}\text{C}$) related to the four climate regimes. The events selected for the composite construction correspond to the winters when the regime is dominant. Only significant points based on a two-sided t-test at the 95% level are shown. Contour interval is 0.2°C .

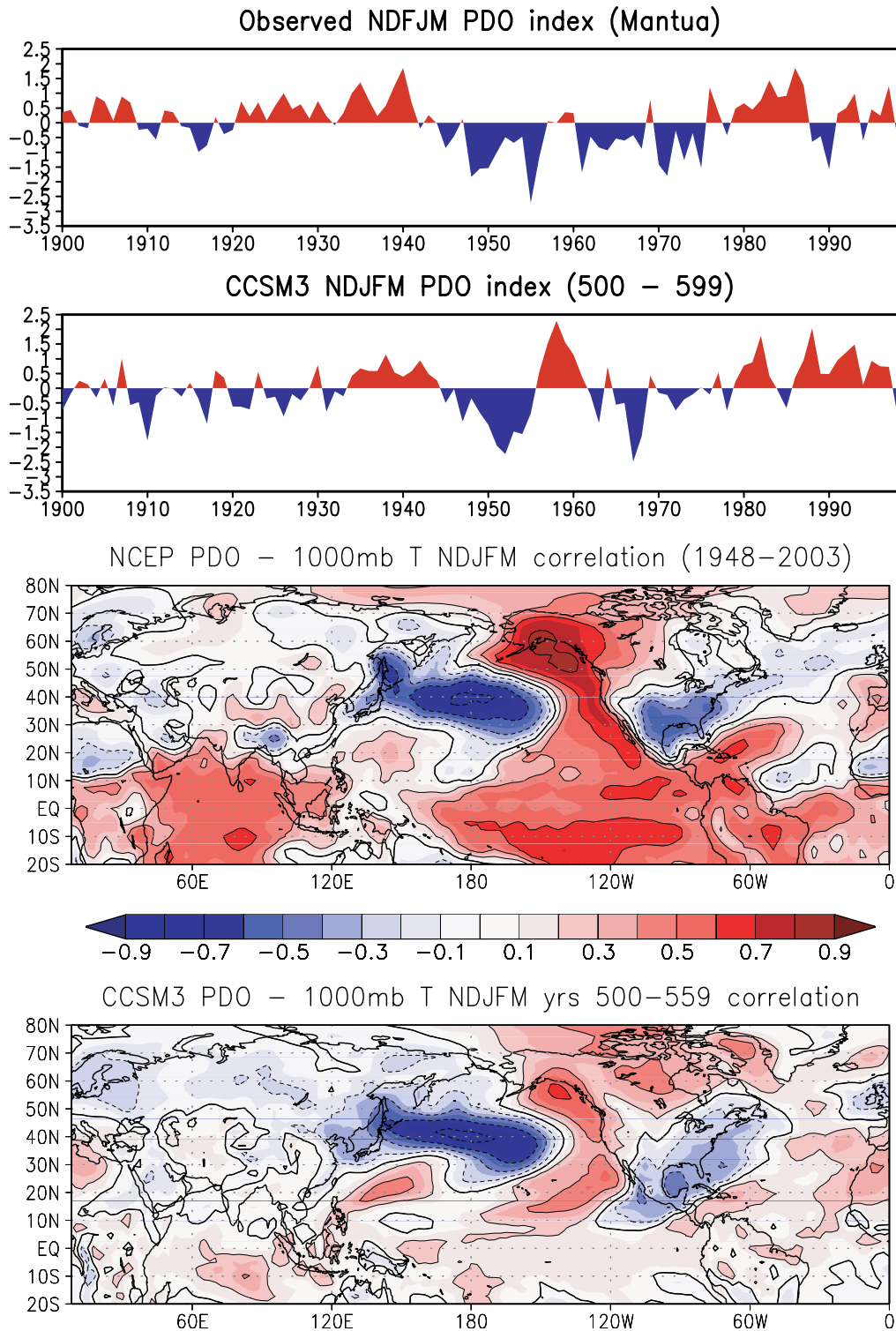


Fig. 14: The a) observed and b) simulated PDO time series in winter, based on the leading principal component of monthly SST anomalies north of 20°N in the Pacific, averaged over November-March. The correlation between the wintertime PDO values and the concurrent near-surface air temperature in c) NCEP reanalysis (1948-2003) and d) the CCSM3 (500-559).

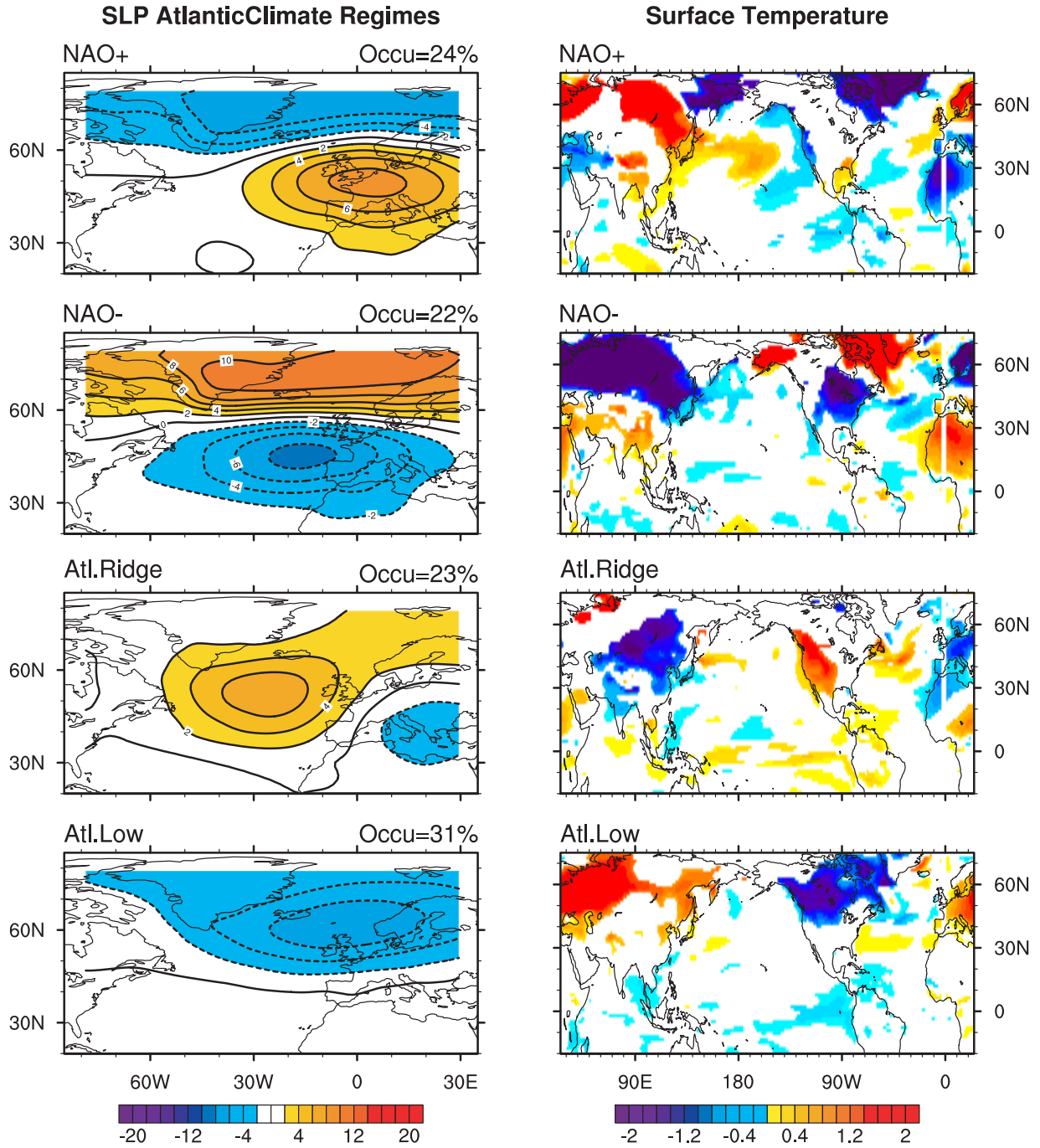


Fig. 15. Same as Fig. 13 but for the regimes in the North Atlantic sector.

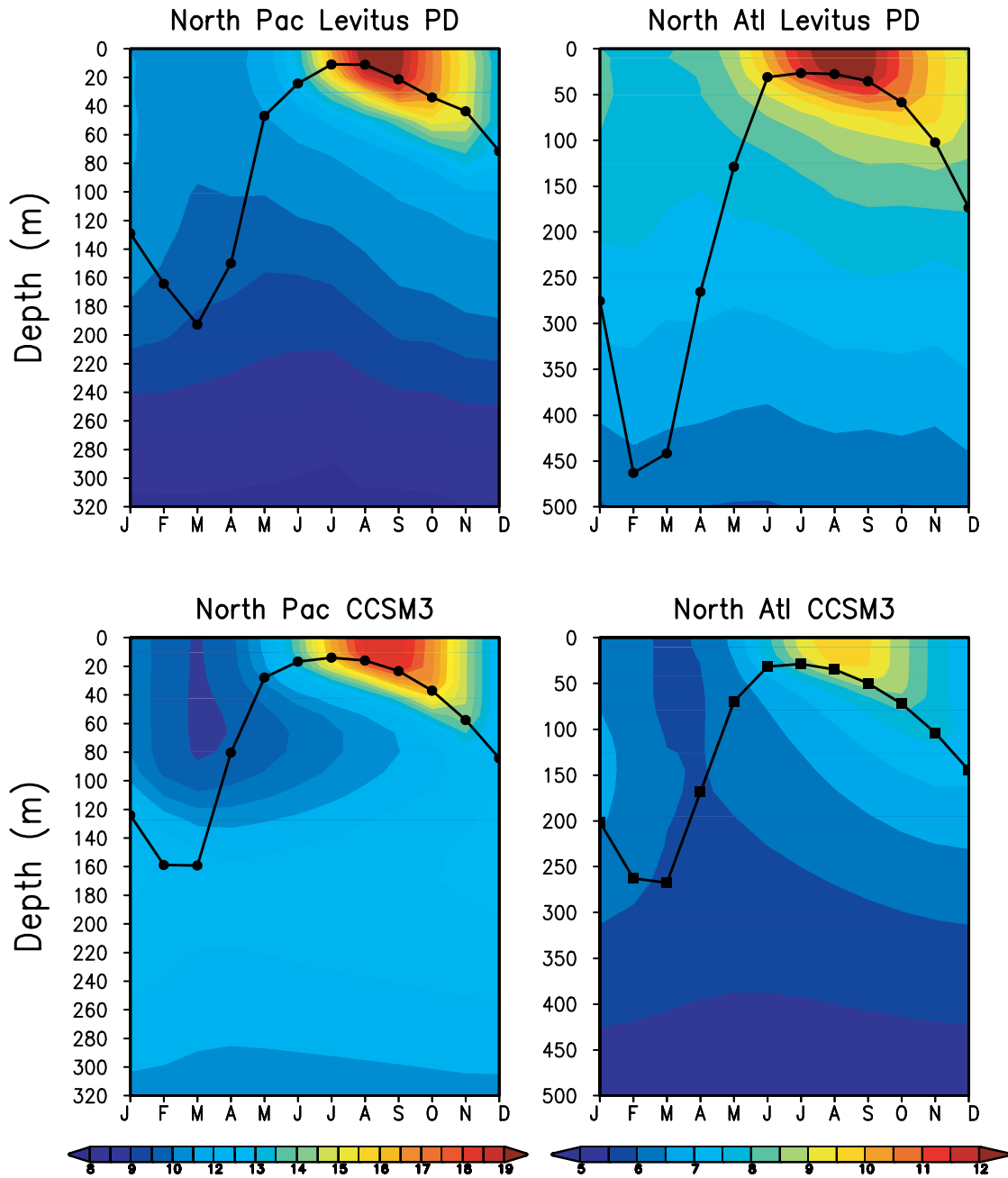


Fig 16. The observed and simulated long term mean seasonal cycle of temperature ($^{\circ}\text{C}$, scale at bottom) and MLD (m) in observations (top) and CCSM3 (bottom) in regions of the central North Pacific (35°N - 45°N , 165°E - 175°W) and North Atlantic (50°N - 60°N , 20°W - 40°W). The observed temperature and MLD values are from the World Ocean Atlas (Levitus et al. 1998) and Monterey and Levitus (1997), respectively and the model results from years 350-599 of CCSM3. The observed and model MLD are both based on density criteria, the former the depth at which the density is 0.125 kg m^{-3} greater than at the surface and the latter is the depth of the maximum gradient that is nearest to the surface. Note that the depth scale is different in the Pacific and Atlantic plots.

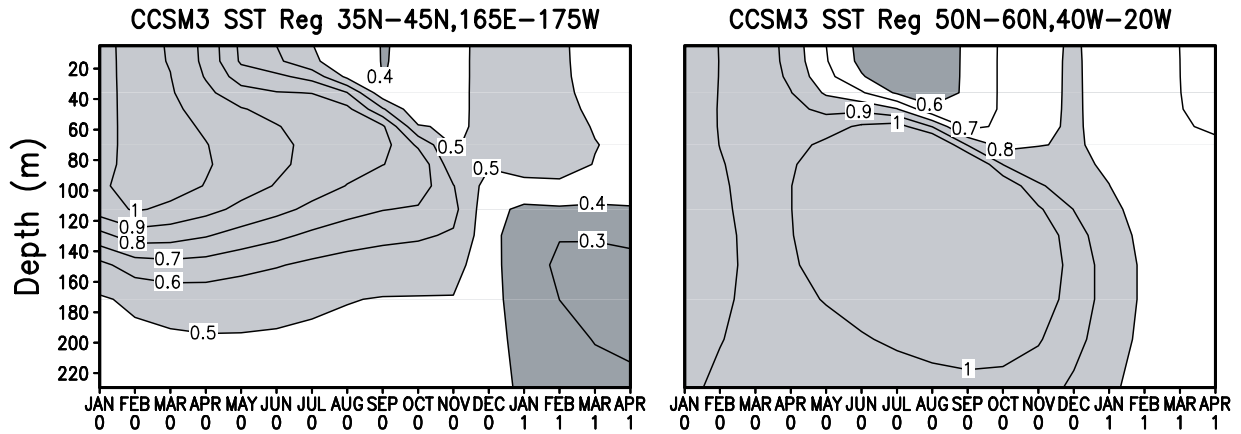


Fig. 17: The reemergence process in the CCSM3 as indicated by lead-lag regressions ($^{\circ}\text{C}$ per 1°C) between temperature anomalies at the base point, defined here as the 3 top ocean model layers (0-30 m) in FMA, and temperature anomalies from the previous January through the following April in the (a) Pacific and (b) Atlantic regions. The contour interval is 0.1 and values >0.5 (<0.4) in (a), and >0.8 (<0.6) in (b) are shaded light (dark).

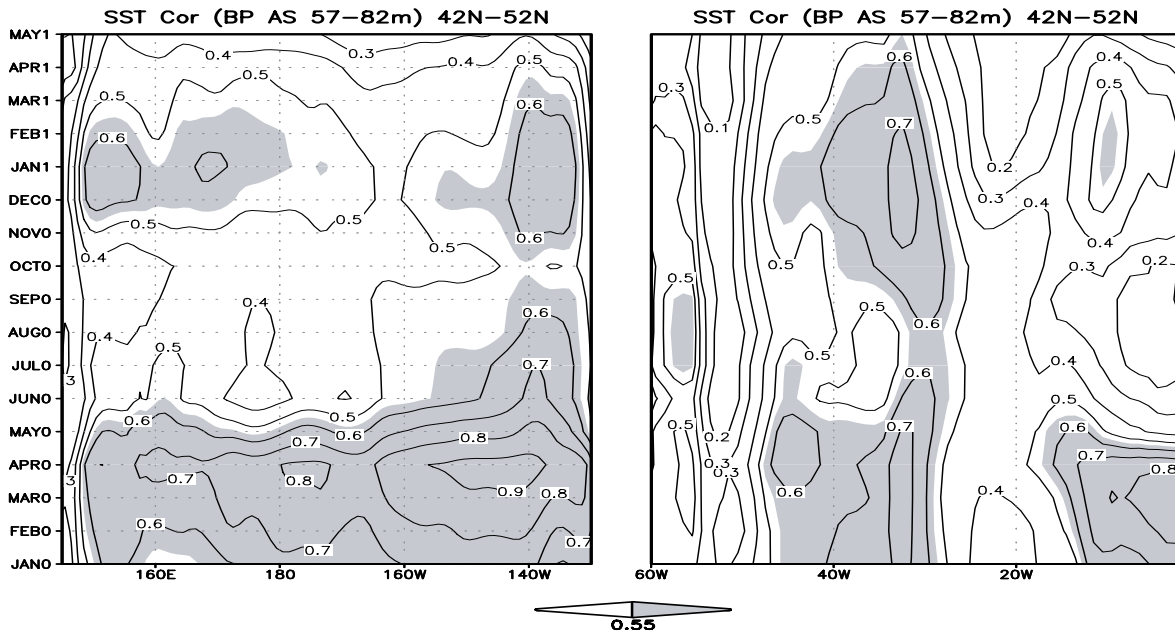


Fig. 18: Basin-wide reemergence in the CCSM3 across the North Pacific (left) and North Atlantic (right) Oceans as indicated by monthly lead-lag correlations between temperature anomalies located between 65-85 m in August-September, and SST anomalies from the previous January through the following April averaged over 42°N-52°N. The contour interval is 0.1, and values greater than 0.55 are shaded.

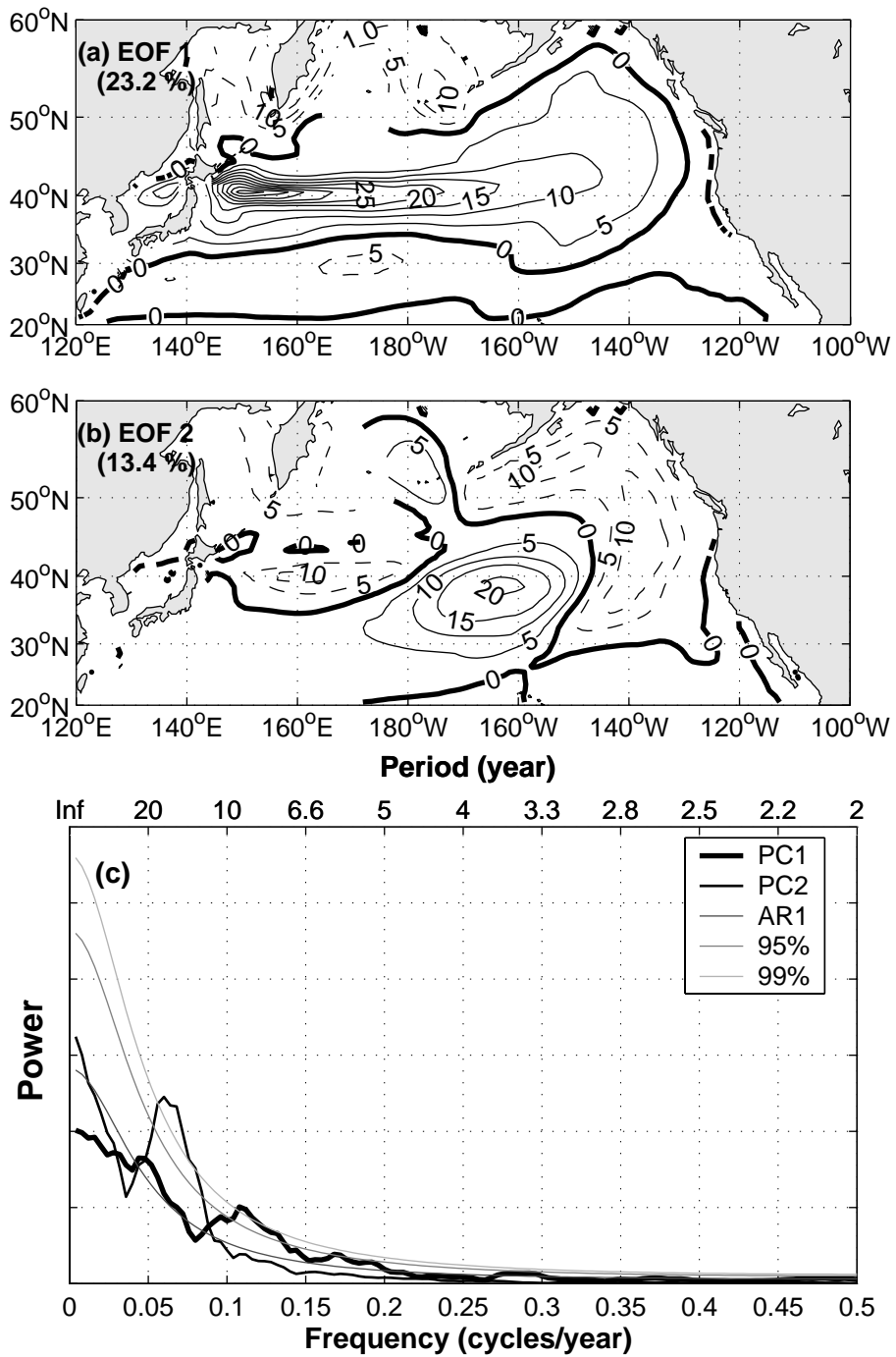


Fig. 19. The (a) first and (b) second EOF of the annual mean depth of the 26.8 σ_θ isopycnal for years 350-599 of the CCSM3 T85 control experiment. Values are relative to a one standard deviation change in the corresponding PC. Contour interval is 5 m in (a) and (b). (c) Power spectrum of PC 1 and 2. Also shown are the best fit AR1 spectra and associated 95% and 99% confidence limits.

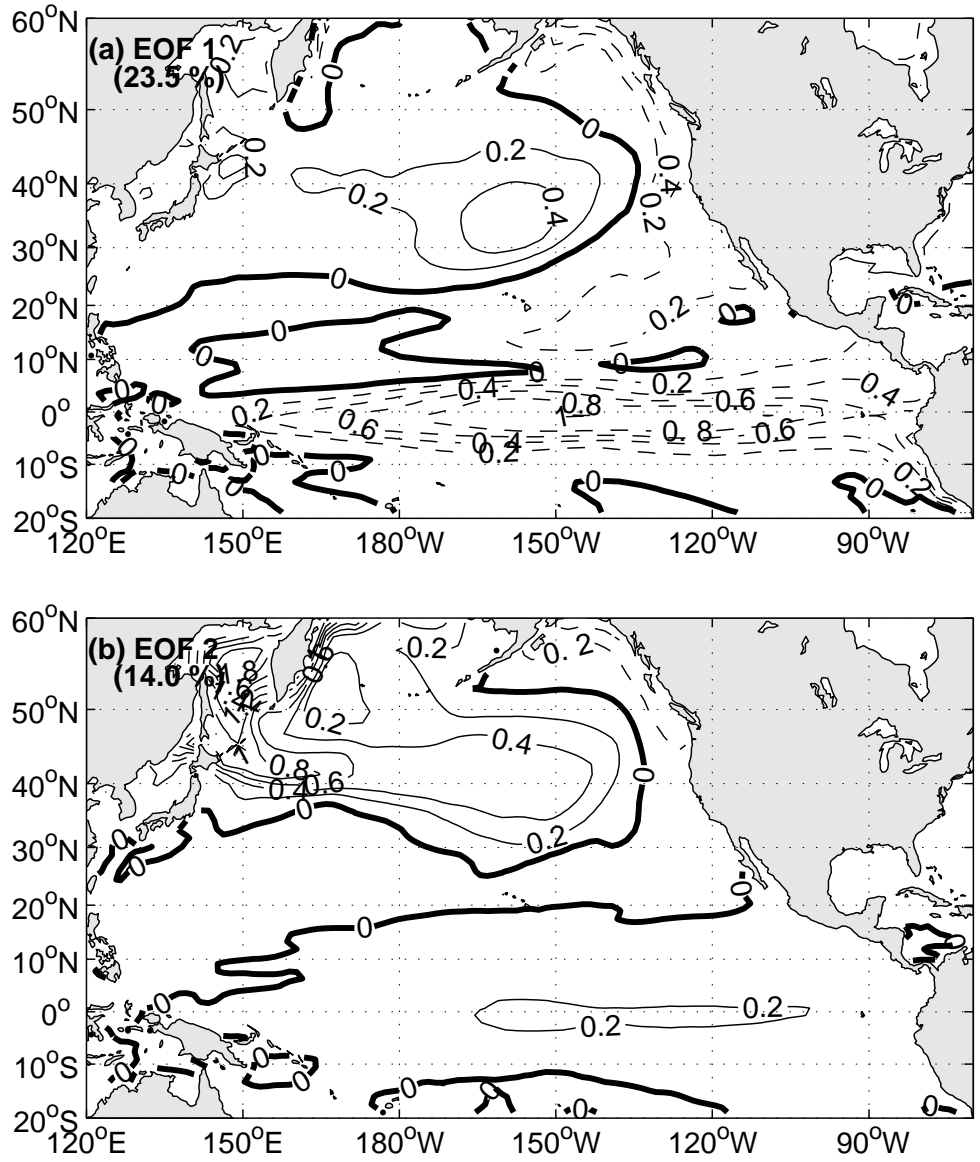


Fig. 20. The (a) first (b) second EOF of the December-March mean SST for years 350-599 of the CCSM3 T85 control experiment. Values are relative to a one standard deviation change in the corresponding PC. The contour interval is 0.2°C.

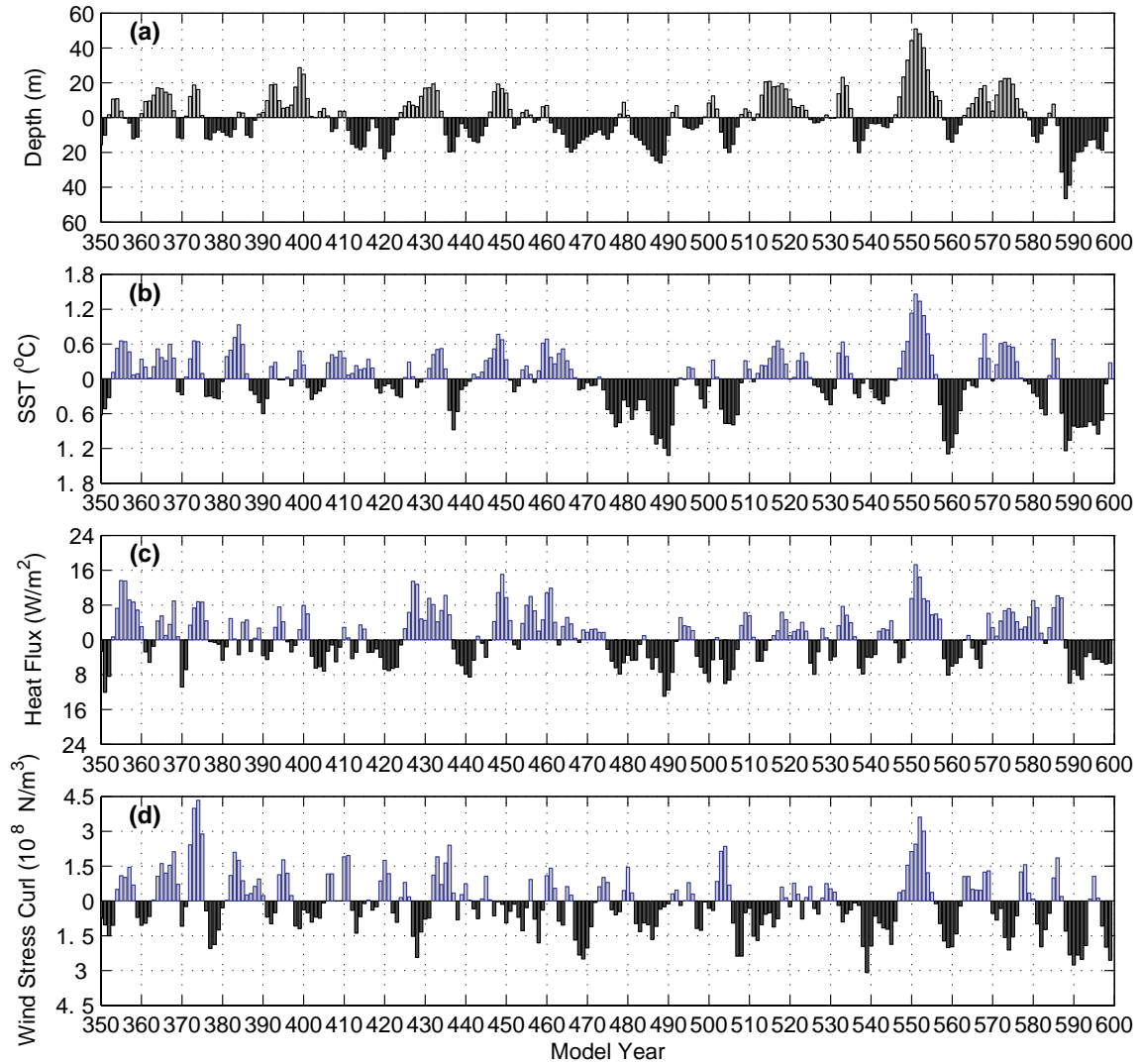


Fig. 21. Indices averaged over the Kuroshio-Oyashio extension region (35°N - 45°N , 140°E - 180°E). (a) Annual mean depth of the $26.8 \sigma_\theta$ isopycnal. (b) Annual mean SST. (c) Annual mean net surface heat flux. Positive value means heat flux anomaly from ocean to the atmosphere. (d) Annual mean wind stress curl. Positive value means counter-clockwise anomalous wind stress curl.

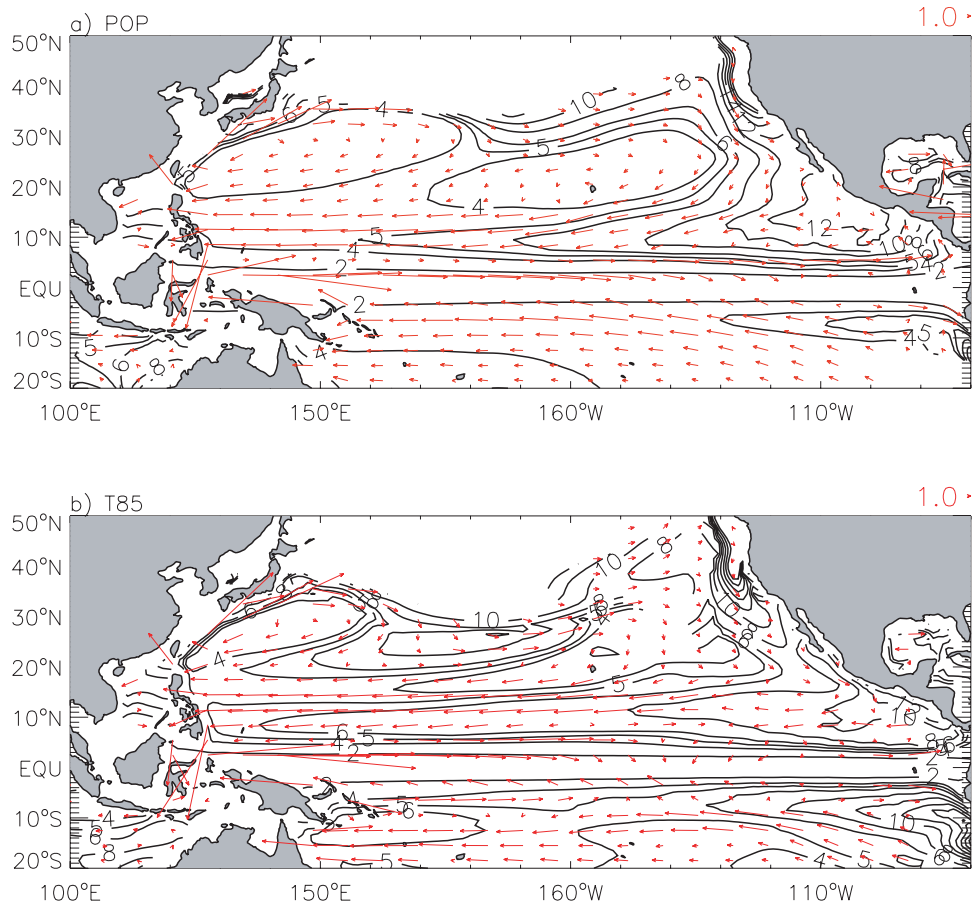


Fig. 22. (a) Absolute value of potential vorticity (in $10^{-10} \text{ m}^{-1} \text{ s}^{-1}$) on the 25 σ_θ potential density surface from POP, the ocean component of the CCSM3, forced with observed surface fields over the period 1958-2000. The flow field in the thermocline, shown by the red vectors, is computed by integrating the horizontal velocity components vertically between the 25.5 and 24.5 σ_θ potential density surfaces. (b) Same as (a), but from the T85 CCSM3 (years 350-400). Potential vorticity is defined as $(f/(\rho_0)) \frac{\partial \rho}{\partial z}$, where f is the Coriolis parameter, $\frac{\partial \rho}{\partial z}$ is the vertical density gradient, and ρ_0 is a reference density (10^3 kg m^{-3}).

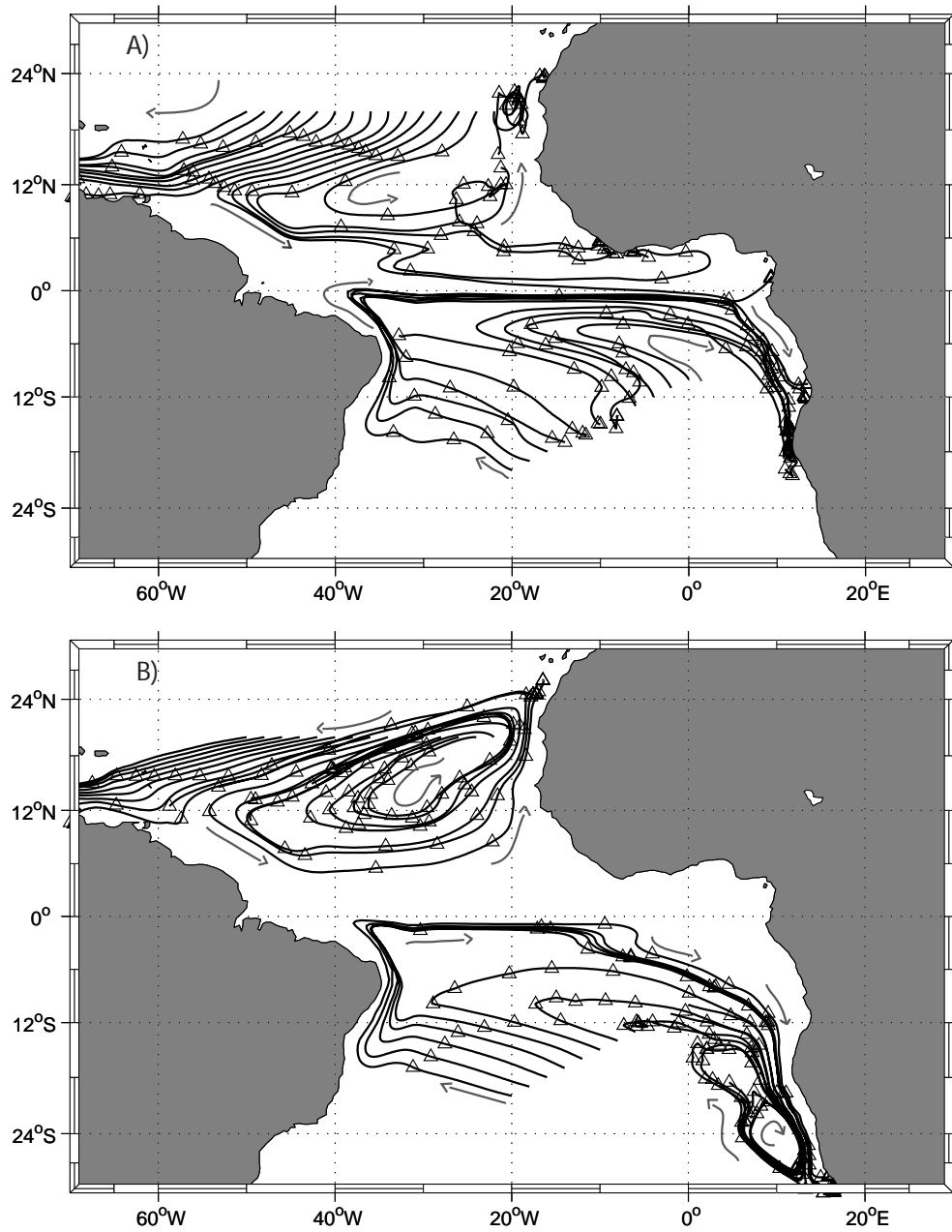


Fig. 23 Lagrangian trajectories along the $25.4 \sigma_\theta$ surface in the a) POP and b) CCSM3 simulations. The trajectories are based on annual averages, the triangles represent the yearly position of floats originally released at the outcrop line in the subtropics, while the vectors indicate the direction of the flow. The trajectories are based on the projection of the velocity field onto an isopycnal surface and, therefore, do not include diapycnal flow.